

1 A mechanistic-statistical approach to infer dispersal and  
2 demography from invasion dynamics, applied to a plant  
3 pathogen

4 Méline Saubin<sup>1</sup>\*, Jérôme Coville<sup>2</sup>, Constance Xhaard<sup>1,2,3</sup>, Pascal Frey<sup>1</sup>,  
Samuel Soubeyrand<sup>2</sup>, Fabien Halkett<sup>1</sup>1# and Frédéric Fabre<sup>4</sup>4#

5 <sup>1</sup> Université de Lorraine, INRAE, IAM, F-54000 Nancy, France

6 <sup>2</sup> INRAE, BioSP, 84914 Avignon, France

7 <sup>3</sup> Université de Lorraine, INSERM CIC-P 1433, CHRU de Nancy, INSERM U1116, Nancy, France

8 <sup>4</sup> INRAE, Bordeaux Sciences Agro, SAVE, F-33882 Villenave d'Ornon, France

9

10 **Corresponding author\*** Current adress: Meline Saubin **Current adress:** Populationsgenetik,  
11 Technische Universität München, Liesel-Beckmann-Str. 2, 85354 Freising, Germany

12 **E-mail:#** These authors co-directed this work.

13 Corresponding authors:

14 Méline Saubin (meline.saubin@tum.de)

15 Fabien Halkett (fabien.halkett@inrae.fr)

16 Frédéric Fabre (frederic.fabre@inrae.fr)

17 **Keywords:** 1-D colonisation, dispersal kernel, long-distance dispersal, multiple data types,  
18 population dynamic, spatio-temporal model

## 19 Abstract

20 Dispersal, and in particular the frequency of long-distance dispersal (LDD) events, has strong im-  
21 plications for population dynamics with possibly the acceleration of the colonisation front, and for  
22 evolution with possibly the conservation of genetic diversity along the colonised domain. How-  
23 ever, accurately inferring LDD is challenging as it requires both large-scale data and a method-  
24 ology that encompasses the redistribution of individuals in time and space. Here, we propose  
25 a mechanistic-statistical framework to estimate dispersal from one-dimensional invasions. The  
26 mechanistic model takes into account population growth and grasps the diversity in dispersal pro-  
27 cesses by using either diffusion, leading to a reaction-diffusion (R.D.) formalism, or kernels, lead-  
28 ing to an integro-differential (I.D.) formalism. The latter considers different dispersal kernels  
29 (*e.g.* Gaussian, Exponential, and Exponential-power) differing in their frequency of LDD events.  
30 The statistical model relies on dedicated observation laws that describe two types of samples,  
31 clumped or not. As such, we take into account the variability in both habitat suitability and oc-  
32 cupancy perception. We first check the identifiability of the parameters and the confidence in  
33 the selection of the dispersal process. We observed good identifiability for ~~nearly~~ all parameters  
34 (~~Correlation Coefficient > 0.95~~ correlation coefficient > 0.9 between true and fitted values), ~~except~~  
35 ~~for occupancy perception (Correlation Coefficient = 0.83–0.85)~~. The dispersal process that is  
36 the most confidently identified is Exponential-Power (*i.e.* fat-tailed) kernel. We then applied our  
37 framework to data describing an annual invasion of the poplar rust disease along the Durance River  
38 valley over nearly 200 km. This spatio-temporal survey consisted of 12 study sites examined at  
39 seven time points. We confidently estimated that the dispersal of poplar rust is best described by  
40 an Exponential-power kernel with a mean dispersal distance of ~~2.01~~ 1.94 km and an exponent

41 parameter of 0.24 characterising a fat-tailed kernel with frequent LDD events. By considering the  
42 whole range of possible dispersal processes our method forms a robust inference framework. It can  
43 be employed for a variety of organisms, provided they are monitored in time and space along a  
44 one-dimension invasion.

45 **Keywords:** 1-D colonisation, dispersal kernel, long-distance dispersal, multiple data types, population  
46 dynamic, spatio-temporal model

# 1 Introduction

Dispersal is key in ecology and evolutionary biology (Clobert et al., 2004). From an applied point of view, the knowledge of dispersal is of prime interest for designing ecological-based management strategies in a wide diversity of contexts ranging from the conservation of endangered species (*e.g.*, Macdonald and Johnson, 2001) to the mitigation of emerging epidemics (Dybiec et al., 2009; Fabre et al., 2021). From a theoretical point of view, the pattern and strength of dispersal sharply impact eco-evolutionary dynamics (*i.e.* the reciprocal interactions between ecological and evolutionary processes) (Miller et al., 2020). The features of dispersal have many implications for population dynamics (*e.g.* speed of invasion, metapopulation turnover; Soubeyrand et al., 2015; Kot et al., 1996), genetic structure (*e.g.* gene diversity, population differentiation; Edmonds et al., 2004; Fayard et al., 2009; Petit, 2011) and local adaptation (Gandon and Michalakis, 2002; Hallatschek and Fisher, 2014). Mathematically, the movement of dispersers (individuals, spores or propagules for example) can be described by a so-called location dispersal kernel (Nathan et al., 2012) that represents the statistical distribution of the locations of the propagules of interest after dispersal from a source point. Since the pioneer works of Mollison (1977), much more attention has been paid to the fatness of the tail of the dispersal kernel (Klein et al., 2006). Short-tailed kernels (also referred to as thin-tailed) generate an invasion front of constant velocity, whereas long-tailed kernels (also referred to as fat-tailed) can cause an accelerating front of colonisation (Ferrandino, 1993; Kot et al., 1996; Clark et al., 2001; Mundt et al., 2009; Hallatschek and Fisher, 2014). Long-tailed kernels, characterised by more frequent long-distance dispersal (LDD) events than an exponential kernel that shares the same mean dispersal distance, can also cause a reshuffling of alleles along the colonisation gradient, which prevents the erosion of genetic diversity (Nichols and Hewitt, 1994; Petit,

69 [2004](#); Fayard et al., [2009](#)) or leads to patchy population structures (Ibrahim et al., [1996](#); Bialozyt  
70 et al., [2006](#)).

71 Despite being a major issue in biology, properly characterising the dispersal kernels is a challen-  
72 ging task for many species, especially when dispersing individuals are numerous, small (and thus  
73 difficult to track) and move far away (Nathan, [2001](#)). In that quest, mechanistic-statistical models  
74 enable a proper inference of dispersal using spatio-temporal datasets (Wikle, [2003a](#); Soubeyrand  
75 et al., [2009a](#); Roques et al., [2011](#); Soubeyrand and Roques, [2014](#); Hefley et al., [2017](#); Nembot  
76 Fomba et al., [2021](#)) while allowing for the parsimonious representation of both growth and dispersal  
77 processes in heterogenous environments (Papaix et al., [2022](#)). They require detailed knowledge of  
78 the biology of the species of interest to properly model the invasion process. They combine a mech-  
79 anistic model describing the invasion process and a probabilistic model describing the observation  
80 process while enabling a proper inference using spatio-temporal data. Classically, the dynamics of  
81 large populations are well described by deterministic differential equations. Invasions have often  
82 been modelled through reaction-diffusion equations (Murray, [2002](#); Okubo and Levin, [2002](#); Shi-  
83 gesada and Kawasaki, [1997](#)). In this setting, individuals are assumed to move randomly following  
84 trajectories modelled using a Brownian motion or a more general stochastic diffusion process. Des-  
85 pite their long standing history, the incorporation of reaction-diffusion equations into mechanistic-  
86 statistical approaches to estimate parameters of interest from spatio-temporal data essentially dates  
87 back to the early 2000s (*e.g.* Wikle, [2003a](#); Soubeyrand and Roques, [2014](#); Louvrier et al., [2020](#);  
88 Nembot Fomba et al., [2021](#)). By contrast to reaction-diffusion equations, integro-differential equa-  
89 tions encode trajectories modelled by jump diffusion processes and rely on dispersal kernels, in-  
90 dividuals being redistributed according to the considered kernel (Fife, [1996](#); Hutson et al., [2003](#);  
91 Kolmogorov et al., [1937](#)). This approach allows to consider a large variety of dispersal functions,

92 typically with either a short or a long tail (*i.e.* putative LDD events). As such it is more likely to  
93 model accurately the true organism's dispersal process. In the presence of long-distance dispersal,  
94 the biological interpretation of the estimated diffusion parameters with an R.D. equation would be  
95 misleading. However, integro-differential equations are numerically more demanding to simulate  
96 than reaction-diffusion equations. As far as we know, integro-differential equations have rarely  
97 been embedded into mechanistic-statistical approaches to infer dispersal processes in ecology (but  
98 see Szymańska et al., 2021 for a recently proposed application of a non-local model to cell prolifer-  
99 ation).

100

101 Data acquisition is another challenge faced by biologists in the field, all the more that data con-  
102 fined to relatively small spatial scales can blur the precise estimates of the shape of the kernels  
103 tail (Ferrandino, 1996; Kuparinen et al., 2007; Rieux et al., 2014). To gather as much information  
104 as possible, it is mandatory to collect data over a wide range of putative population sizes (from  
105 absence to near saturation) along the region of interest. Sharing the sampling effort between raw  
106 and refined samples to browse through the propagation front may improve the inference of spatial  
107 ecological processes (Gotway and Young, 2002). This way of sampling is all the more interesting  
108 as the probabilistic model describing the observation process in the mechanistic-statistical approach  
109 can handle such multiple datasets (Wikle, 2003b). However, inference based on multi-type data  
110 remains a challenging statistical issue as the observation variables describing each data type follow  
111 different distribution laws (Chagneau et al., 2011) and can be correlated or, more generally, depend-  
112 ent because they are governed by the same underlying dynamics (Bourgeois et al., 2012; Georgescu  
113 et al., 2014; Soubeyrand et al., 2018). This requires a careful definition of the conditional links  
114 between the observed variables and the model parameters (the so-called observation laws) in order

115 to identify and examine complementarity and possible redundancy between data types.

116

117 In this article, we aim to provide a sound and unified inferential framework to estimate dispersal  
118 from ecological invasion data using both reaction-diffusion and integro-differential equations. We  
119 first define the two classes of mechanistic invasion models, establish the observation laws corres-  
120 ponding to raw and refined samplings, and propose a maximum-likelihood method to estimate their  
121 parameters within the same inferential framework. Then, to confirm that each model parameter  
122 can indeed be efficiently estimated given the amount of data at hand (see Soubeyrand and Roques,  
123 2014), we perform a simulation study to check model parameters' identifiability given the sampling  
124 design. We also aim to assess the confidence level in the choice of the dispersal function as derived  
125 by model selection. Last, the inferential framework is applied to original ecological data describing  
126 the annual invasion of a tree pathogen (*Melampsora larici-populina*, a fungal species responsible  
127 for the poplar rust disease) along the riparian stands of wild poplars bordering the Durance River  
128 valley in the French Alps (Xhaard et al., 2012).

## 129 **2 Modelling one-dimensional invasion and observation processes**

### 130 **2.1 A class of deterministic and mechanistic invasion models**

131 We model the dynamics of a population density  $u(t, x)$  at any time  $t$  and point  $x$  during an invasion  
132 using two types of spatially heterogeneous deterministic models allowing to represent a wide range  
133 of dispersal processes. Specifically, we considered a reaction-diffusion model (R.D.) and an integro-  
134 differential model (I.D.):



$$\begin{array}{l}
135 \\
136
\end{array}
\left\{ \begin{array}{l}
\text{R.D.} \left\{ \begin{array}{l} \partial_t u(t,x) = D \partial_{xx} u(t,x) + r(x) u(t,x) \left( 1 - \frac{u(t,x)}{K} \right), \\ u(0,x) = u_0(x), \end{array} \right. \\
\text{I.D.} \left\{ \begin{array}{l} \partial_t u(t,x) = \int_{-R}^R J(x-y) [u(t,y) - u(t,x)] dy + r(x) u(t,x) \left( 1 - \frac{u(t,x)}{K} \right), \\ u(0,x) = u_0(x). \end{array} \right.
\end{array} \right.$$

137 where  $t$  varies in  $[0, T]$  (*i.e.* the study period) and  $x$  varies in  $[-R, R]$  (*i.e.* the study domain). Both  
138 equations exhibit the same structure composed of a diffusion/dispersal component and a reaction  
139 component. The reaction component,  $r(x) u(t,x) \left( 1 - \frac{u(t,x)}{K} \right)$  in both equations, is parameterised  
140 by a spatial growth rate  $r(x)$  that takes into account macro-scale variations of the factors regulat-  
141 ing the population density and  $K$  the carrying capacity of the environment. It models population  
142 growth. The diffusion/dispersal component models population movements either by a diffusion  
143 process ( $D \partial_{xx} u$  in R.D.) parameterised by the diffusion coefficient  $D$  or by a dispersal kernel ( $J$  in  
144 I.D.). To cover a large spectrum of possible dispersal processes, we use the following parametric  
145 form for the kernel  $J$ :

$$J := \frac{\tau}{2\alpha\Gamma\left(\frac{1}{\tau}\right)} e^{-\left|\frac{z}{\alpha}\right|^\tau} \quad (1)$$

146 with mean dispersal distance  $\lambda := \alpha \frac{\Gamma\left(\frac{2}{\tau}\right)}{\Gamma\left(\frac{1}{\tau}\right)}$ . Varying the value of  $\tau$  leads to the kernels classically  
147 used in dispersal studies. Specifically,  $J$  can be a Gaussian kernel ( $\tau = 2, \lambda = \alpha/\sqrt{\pi}$ ), an exponen-  
148 tial kernel ( $\tau = 1, \lambda = \alpha$ ) or a fat-tail kernel ( $\tau < 1, \lambda = \alpha\Gamma\left(\frac{2}{\tau}\right)/\Gamma\left(\frac{1}{\tau}\right)$ ). Explicit formulas for  
149 the solution  $u(t,x)$  of these reaction-diffusion/dispersal equations being out of reach, we compute a  
150 numerical approximation  $u_{\text{num}}$  of  $u$ , which serves as a surrogate for the real solution. Details of the  
151 numerical scheme used to compute  $u_{\text{num}}$  can be found in Appendix S1.

## 2.2 A conditional stochastic model to handle micro-scale fluctuations

Among the factors driving population dynamics, some are structured at large spatial scales (macro-scale) and others at local scales (micro-scale). It is worth considering both scales when studying biological invasions. In the model just introduced, the term  $r(x)$  describes factors impacting population growth rate at the macro-scale along the whole spatial domain considered. Accordingly, the function  $u(t, x)$  is a mean-field approximation of the true population density at macro-scale. Furthermore, the population density can fluctuate due to micro-scale variations of other factors regulating population densities locally (*e.g.* because of variations in the micro-climate and the host susceptibility). Such local fluctuations are accounted for by a conditional probability distribution on  $u(t, x)$ , the macro-scale population density, which depends on the (unobserved) suitability of the habitat unit as follow. Consider a habitat unit  $i$  whose centroid is located at  $x_i$ , and suppose that the habitat unit is small enough to reasonably assume that  $u(t, x) = u(t, x_i)$  for every location  $x$  in the habitat unit. Let  $N_i(t)$  denote the number of individuals in  $i$  at time  $t$ . The conditional distribution of  $N_i(t)$  is modelled by a Poisson distribution:

$$N_i(t) \mid u(t, x_i), R_i(t) \sim \text{Poisson}(u(t, x_i)R_i(t)), \quad (2)$$

where  $R_i(t)$  is the intrinsic propensity of the habitat unit  $i$  to be occupied by individuals of the population at time  $t$ . Thereafter,  $R_i(t)$  is called habitat suitability and takes into account factors like the exposure and the favorability of habitat unit  $i$ . The suitability of habitat unit  $i$  is a random effect (unobserved variable) and is assumed to follow a Gamma distribution with shape parameter  $\sigma^{-2}$  and scale parameter  $\sigma^2$ :

$$R_i(t) \sim \text{Gamma}(\sigma^{-2}, \sigma^2). \quad (3)$$

171 This parametrisation implies that the mean and variance of  $R_i(t)$  are 1 and  $\sigma^2$ , respectively; that the  
 172 conditional mean and variance of  $N_i(t)$  given  $u(t, x_i)$  are  $u(t, x_i)$  and  $u(t, x_i) + u(t, x_i)^2 \sigma^2$ , respect-  
 173 ively; and that its conditional distribution is:

$$N_i(t) | u(t, x_i) \sim \text{Negative-Binomial} \left( \sigma^{-2}, \frac{u(t, x_i) \sigma^2}{1 + u(t, x_i) \sigma^2} \frac{1}{1 + u(t, x_i) \sigma^2} \right). \quad (4)$$

### 174 **2.3 Multi-type sampling and models for the observation processes**

175 During an invasion, the population density may range from zero (beyond the front) to the maximum  
 176 carrying capacity of the habitat. To optimise the sampling effort, it may be relevant to carry out  
 177 different sampling procedures depending on the population density at the sampling sites. In this  
 178 article, we consider a two-stage sampling made of one raw sampling, which is systematic and one  
 179 optional refined sampling adapted to our case study, the downstream spread of a fungal pathogen  
 180 along a river (Figure 1). We consider that the habitat unit is a leaf. The fungal population is  
 181 monitored in sampling sites  $s \in \{1, \dots, S\}$  and at sampling times  $t \in \{t_1, \dots, t_K\}$ . Sampling sites are  
 182 assumed to be small with respect to the study region, and the duration for collecting one sample  
 183 is assumed to be short with respect to the study period. Thus, the (macro-scale) density of the  
 184 population at sampling time  $t$  in sampling site  $s$  is constant and equal to  $u(t, z_s)$  where  $z_s$  is the  
 185 centroid of the sampling site  $s$ . Any sampling site  $s$  is assumed to contain a large number of leaves  
 186 which are, as a consequence of the assumptions made above, all associated with the same population  
 187 density function:  $u(t, x_i) = u(t, z_s)$  for all leaves  $i$  within sampling site  $s$ . Each observed tree and twig  
 188 are assumed to be observed only once during the sampling period. Therefore, habitat suitabilities  
 189  $R_i(t)$  are considered independent in time.

190 The raw sampling is focused on trees, considered as a group of independent leaves regarding  
191 their suitabilities. This assumption can be made if the leaves observed on the same tree are suffi-  
192 ciently far from each other and represent a large variety of environmental conditions, and therefore  
193 habitat suitabilities (for example, leaves observed all around a tree will not have the same sun ex-  
194 position, nor the same humidity depending on their height and their relative positions to the trunk).  
195 In each sampling site  $s$  and at each sampling time  $t$ , a number  $B_{st}$  of trees are monitored for the  
196 presence of infection. We count the number of infected trees  $Y_{st}$  among the total number  $B_{st}$  of  
197 observed trees. In the simulations and the case study tackled below, the random variables  $Y_{st}$  given  
198  $u(t, x_s)$  are independent and distributed under the conditional Binomial distribution  $f_{st}^{\text{raw}}$  described  
199 in Appendix S2.2. Its success probability depends on the variabilities of (i) the biological process  
200 through the variance parameter  $\sigma^2$  of habitat suitabilities, and (ii) the observation process through  
201 a parameter  $\gamma$ . This parameter describes how the probabilities of leaf infection perceived by the  
202 person in charge of the sampling differ between trees from true probabilities (as informed by the  
203 mechanistic model). Such differences may be due, for example, to the specific configuration of the  
204 canopy of each tree or to particular lighting conditions.

205 The refined sampling is focused on twigs, considered as a group of connected leaves. Nearby  
206 leaves often encounter the same environmental conditions and, therefore, are characterised by sim-  
207 ilar habitat suitabilities represented by  $R_i(t)$ ; see Equations (2–3). This spatial dependence was  
208 taken into account by assuming that the leaves of the same twig (considered as a small group of  
209 spatially connected leaves) share the same leaf suitability. Accordingly, suitabilities are considered  
210 as shared random effects. The refined sampling is performed depending on disease prevalence and  
211 available time. In site  $s$  at time  $t$ ,  $G_{st}$  twigs are collected. For each twig  $g$ , the total number of  
212 leaves  $M_{stg}$  and the number of infected leaves  $Y_{stg}$  are counted. In the simulations and the case

213 study tackled below, the random variables  $Y_{stg}$  given  $u(t, x_s)$  are independent and distributed under  
 214 conditional probability distributions denoted by  $f_{st}^{\text{ref}}$  described in Appendix S2.3. The distribution  
 215  $f_{st}^{\text{ref}}$  is a new mixture distribution (called Gamma-Binomial distribution) obtained using Equations  
 216 (2–3) and taking into account the spatial dependence and the variance parameter of unobserved  
 217 suitabilities (see Appendix S2.3).

218 This sampling scheme and its vocabulary (leaves, twigs and trees) are specifically adapted to  
 219 our case study for the sake of clarity. However, a wide variety of multi-type sampling strategies can  
 220 be defined and implemented in the model, as long as it fits a two-stage sampling as presented in  
 221 Figure 1.

## 222 2.4 Coupling the mechanistic and observation models

223 The submodels of the population dynamics and the observation processes described above can be  
 224 coupled to obtain a mechanistic-statistical model (also called physical-statistical model; Berliner,  
 225 2003; Soubeyrand et al., 2009b) representing the data and depending on dynamical parameters,  
 226 namely the growth and dispersal parameters. The likelihood of this mechanistic-statistical model  
 227 can be written:

$$L(\theta) = \prod_{s=1}^S \prod_{t=t_1}^{t_K} \left\{ f_{st}^{\text{raw}}(Y_{st}) \left( \prod_{g=1}^{G_{st}} f_{st}^{\text{ref}}(Y_{stg}) \right)^{\mathbb{1}(Y_{st} > \bar{y})} \right\}, \quad (5)$$

228 where  $\mathbb{1}(\cdot)$  denotes the indicator function and expressions of  $f_{st}^{\text{raw}}$  and  $f_{st}^{\text{ref}}$  adapted to the case study  
 229 tackled below are given by Equations (S14) and (S18) in Appendix S2. The power  $\mathbb{1}(Y_{st} > \bar{y})$  equals  
 230 to 1 if  $Y_{st} > \bar{y}$  and 0 otherwise, implies that the product  $\prod_{g=1}^{G_{st}} f_{st}^{\text{ref}}(Y_{stg})$  only appears if the refined  
 231 sampling is carried out in site  $s$ . Moreover, such a product expression for the likelihood is achieved  
 232 by assuming that leaves in the raw sampling and those in the refined sampling are not sampled from

233 the same trees. If this does not hold, then an asymptotic assumption like the one in Appendix S2.2  
234 can be made to obtain Equation (5), or the dependence of the unobserved suitabilities must be taken  
235 into account and another likelihood expression must be derived.

### 236 **3 Parameter estimation and model selection**

237 We performed simulations to check the practical identifiability of several scenarios of biological  
238 invasions. Invasion scenarios represent a wide range of possible states of nature regarding the  
239 dispersal process, the environmental heterogeneity at macro-scale, and the intensity of local fluctu-  
240 ations at micro-scale. Even though the simulations are designed to cope with the structure of our  
241 real data set (Appendix S4), the results enable some generic insights to be gained. Specifically, we  
242 considered six sampling dates evenly distributed in time and 12 samplings sites evenly distributed  
243 within the 1D spatial domain. For each pair (*date*, *site*), we simulated the raw sampling of 100 trees  
244 and the refined sampling of 20 twigs. For the fifth sampling date, the raw sampling was densified  
245 with 45 sampling sites instead of 12.

246 The simulation study explored four hypotheses for the dispersal process: three I.D. hypotheses  
247 with kernels  $J_{\text{Exp}}$ ,  $J_{\text{Gauss}}$  and  $J_{\text{ExpP}}$  and the R.D. hypothesis. Hypotheses  $J_{\text{Exp}}$  and  $J_{\text{Gauss}}$  state that  
248 individuals dispersed according to Exponential and Gaussian kernels, respectively, with parameter  
249  $\theta_J = (\lambda)$ . Hypothesis  $J_{\text{ExpP}}$  states that individuals dispersed according to a fat-tail Exponential-  
250 power kernel with parameters  $\theta_J = (\lambda, \tau)$  and  $\tau < 1$ . Finally, hypothesis R.D. states that individual  
251 dispersal is a diffusion process parameterised by  $\theta_J = (\lambda)$ . The parameter  $\lambda$  represents the mean  
252 distance travelled whatever the dispersal hypothesis considered. Moreover, macro-scale environ-  
253 mental heterogeneity was accounted for in the simulations by varying the intrinsic growth rate of

254 the pathogen population ( $r$ ) in space. Specifically, along the one-dimensional domain, we con-  
255 sidered two values of  $r$ , namely a downstream value  $r_{\text{dw}}$  and an upstream value  $r_{\text{up}}$ , parameterised  
256 by  $\theta_r = (r_{\text{dw}}, \omega)$  such that  $r_{\text{up}} = r_{\text{dw}}e^\omega$ . Finally, micro-scale heterogeneity was accounted for in  
257 the simulations by varying the parameter of leaf suitability  $\sigma^2$  and tree perception  $\gamma$ . Thereafter,  
258  $\theta = (\theta_r, \theta_J, \gamma, \sigma^2)$  denotes the vector of model parameters.

### 259 **3.1 Accurate inference of model parameters**

260 To assess the estimation method and check if real data that were collected are informative enough  
261 to efficiently estimate the parameters of the models (the so-called practical identifiability), we pro-  
262 ceeded in three steps for each dispersal hypothesis: (i) a set of parameter values  $\theta = (\theta_r, \theta_J, \gamma, \sigma^2)$   
263 is randomly drawn from a distribution that encompasses a large diversity of realistic invasions, (ii)  
264 a data set with a structure similar to our real sampling is simulated given  $\theta$  and (iii)  $\theta$  is estimated  
265 using the maximum-likelihood method applied to the simulated data set. These steps were repeated  
266  ~~$n = 100$~~   $n = 160$  times. Details on the simulation procedure, the conditions used to generate realistic  
267 invasions, and on the estimation algorithm are provided in Appendix S4.1. Practical identifiability  
268 was tested by means of correlation coefficients between the true and estimated parameter values  
269 (see Table 1, Appendix S2: Figures S2, S3, S4, S5).

270 All the parameters defining the macro-scale mechanistic invasion model ( $r_{\text{dw}}$ ,  $\omega$ ,  $\lambda$ ) display  
271 very good practical identifiability whatever the model, with correlation coefficients above ~~0.93~~ 0.98  
272 (except for mean dispersal distance  $\lambda$  under R.D., correlation coefficient of 0.94). In the case of the  
273 Exponential-power dispersal kernel, the additional parameter representing the tail of the distribu-  
274 tion ( $\tau$ ) also displays a very good practical identifiability with a correlation coefficient of ~~0.95~~ 0.93.

275 The parameter defining the micro-scale fluctuations,  $\sigma^2$ , leads to particularly high correlation coef-  
276 ficients (0.99 for all the models). The identifiability for the perception parameter  $\gamma$  related to the  
277 observation process is somewhat lower (from ~~0.83 to 0.85~~ 0.91 to 0.97).

### 278 **3.2 Confidence in the selection of the dispersal process**

279 Numerical simulations were next designed to test whether model selection could disentangle the  
280 true dispersal process (*i.e.* the dispersal hypothesis used to simulate the data set) from alternative  
281 dispersal processes (Appendix S4.2). The model selection procedure is the most efficient for the  
282 dispersal hypotheses Exponential-power  $J_{\text{ExpP}}$ , ~~Exponential  $J_{\text{Exp}}$ , and reaction-diffusion R.D., with~~  
283 ~~70%, 62% and 58%~~ with 78% of correct kernel selection, respectively (Table 2). When the fat-tail  
284 Exponential-power kernel is not correctly identified, it is mostly mistaken with the Exponential one  
285 (for ~~20%~~ 17% of the simulations). In line with this, the probability of correctly selecting the kernel  
286  $J_{\text{ExpP}}$  decreases when the parameter  $\tau$  increases towards 1, the value for which the Exponential-  
287 power kernel coincides with the Exponential kernel (Figure 2). Importantly, when the Exponential-  
288 power kernel is correctly selected, we observe a large difference between its AIC and the AIC of  
289 the second best model (~~89.62~~ 217.50 points on average). Conversely, when the invasion process  
290 is simulated under  $J_{\text{ExpP}}$ , but another kernel is selected, we observe a very small AIC difference  
291 (~~0.38~~ 0.76 point on average). ~~Model selection does not allow to correctly select the~~ The model  
292 selection is the least efficient for the Gaussian kernel  $J_{\text{Gauss}}$  (Table 2). ~~Indeed,~~ with only ~~26%~~ 45%  
293 of correct model selection, ~~this kernel is not better identified than with a random draw of one of the~~  
294 ~~four models, which would lead to 25% of correct estimations.~~ Its correct identification is greatly  
295 ~~improved~~ improved to 80% by densifying the sampling scheme (Appendix S4.5: Table S2). Finally,



296 note that when the invasion process is simulated under model R.D. or  $J_{\text{Gauss}}$ , a short-tail kernel is  
297 almost always selected and, thus, never confounded with the fat-tail kernel  $J_{\text{ExpP}}$ .

## 298 **4 Case study: Invasion of poplar rust along the Durance River** 299 **valley**

### 300 **4.1 Study site**

301 We applied our approach to infer the dispersal of the plant pathogen fungus *Melampsora larici-*  
302 *populina*, responsible for the poplar rust disease, from the monitoring of an epidemic invading  
303 the Durance River valley. Embanked in the French Alps, the Durance River valley constitutes a  
304 one-dimension ecological corridor that channels annual epidemics of the poplar rust pathogen *M.*  
305 *larici-populina* (Xhaard et al., 2012). Each year the fungus has to reproduce on larches (*Larix*  
306 *decidua*) that are located in the upstream part of the valley only. This constitutes the starting point  
307 of the annual epidemics. Then the fungus switches to poplar leaves and performs several rounds of  
308 infection until leaf-fall. Each infected leaf produces thousands of spores that are wind-dispersed. In  
309 our case study,  $u(t, x_s)$  is the density of fungal infection at time  $t$  at point  $x$  on a poplar leaf. Each  
310 leaf has a carrying capacity of 750 fungal infections (Appendix S5).

311 All along the valley, the Durance River is bordered by a nearly continuous riparian forest of  
312 wild poplars (*Populus nigra*). The annual epidemic on poplars thus spreads downstream through the  
313 riparian stands, mimicking a one-dimension biological invasion (Xhaard et al., 2012). A previous  
314 genetic study showed that the epidemic was indeed initiated in an upstream location where poplars  
315 and larches coexist (Prelles), and progresses along the valley (Becheler et al., 2016). In autumn,

316 the corridor is cleared for disease after leaf-fall. At 62 km downstream of the starting point of the  
317 epidemics, the Serre-Ponçon dam represents a shift point in the valley topology, with a steep-sided  
318 valley upstream and a larger riparian zone downstream. This delimitation led us to consider 2 values  
319 of growth rates  $r$  along the one-dimensional domain:  $r_{\text{up}}$  and  $r_{\text{dw}}$  (see Appendix S4 for details).

## 320 **4.2 Monitoring of an annual epidemic wave**

321 In 2008, rust incidence was monitored every three weeks from July to November at 12 sites evenly  
322 distributed along the valley (Figure 3). Sites were inspected during seven rounds of surveys. For a  
323 unique date (Oct. 22), the raw sampling was densified with 45 sites monitored instead of 12. We  
324 focused on young poplar trees (up to 2m high) growing on the stands by the riverside.

325 Two monitorings were conducted, corresponding to the raw and refined sampling, as described  
326 in previous sections. For the raw sampling, we prospected each site at each date to search for rust  
327 disease by inspecting randomly distributed poplar trees (different trees at different dates for a given  
328 site). Depending on rust incidence and poplar tree accessibility, 40 to 150 trees (mean 74) were  
329 checked for disease. Each tree was inspected through a global scan of the leaves on different twigs  
330 until at least one infected leaf was found or after 30 s of inspection. The tree was denoted infected  
331 or healthy, respectively. This survey method amounts to minutely inspecting 10 leaves per tree,  
332 *i.e.* with the same efficiency of disease detection as through the refined sampling (see details of the  
333 statistical procedure in Appendix S3). The global scan procedure of the trees leads to equivalently  
334 surveying fewer and fewer leaves as the epidemic progresses. Optionally, when at least one tree  
335 was infected, and depending on available time, we carried out a refined sampling to collect more  
336 information on the variance in disease susceptibility (*i.e.* habitat suitability) among the sampling

337 domain. The refined sampling consisted in randomly sampling 20 twigs on different trees and  
338 recording, for each, the total number of leaves and the number of infected leaves.

### 339 **4.3 Dispersal and demographic processes ruling the epidemic wave**

340 Model selection was used to decipher which dispersal process was best supported by the data set  
341 for five initial parameter values. The large AIC difference in favour of hypothesis  $J_{\text{ExpP}}$  indicates  
342 that poplar rust propagules assuredly disperse according to an exponential-power dispersal kernel  
343 along the Durance River valley (Table 3). Note that for all kernels, the five initial parameter values  
344 lead to similar estimations. ~~Under the R.D. hypothesis, however, initial parameter values can lead~~  
345 ~~to different estimations because of local optima, but all AIC resulting from the R.D. hypothesis are~~  
346 ~~higher than AIC resulting from the three dispersal kernels.~~

347 The estimation of the parameters for the best model along with their confidence intervals (Ap-  
348 pendix S4.3) are summarised in Table 4. The parameters of the Exponential-power kernel firstly in-  
349 dicate that the mean distance travelled by rust spores is estimated at ~~2.01~~ 1.94 km. Second, its mean  
350 exponent parameter  $\tau$  is 0.24. This value, much lower than 1, suggests substantial long-distance  
351 dispersal events. We also estimated the growth rates of the poplar rust epidemics along the Durance  
352 River valley. From upstream to downstream, their mean estimates are ~~0.084 and 0.020~~ 0.085 and  
353 0.023, respectively. The estimate of the parameter of the observation model,  $\gamma$ , is ~~5.21~~ 4.82. This  
354 parameter represents how perceived probabilities of leaf infection differ among trees from true prob-  
355 abilities. The estimated value of ~~5.21~~ 4.82 indicates some variability in the perception of infected  
356 leaves, but this variability is moderate because the shape of the underlying Beta-Binomial distri-  
357 bution approaches the Binomial distribution (for which perception differences are absent) (Figure

358 4, row 1). By contrast, the estimated value of the micro-scale fluctuation variance  $\sigma^2$  (~~1.09~~1.29)  
359 suggests a substantial variability in leaf suitability between twigs. This is evidenced by comparing  
360 the shape of the estimated Gamma-Binomial distribution with a situation with negligible differences  
361 in receptivity between twigs (Figure 4, row 2, case  $\sigma^2 = 0.01$ ).

362 Model check consists in testing whether the selected model was indeed able –given the para-  
363 meter values inferred above– to reproduce the observed data describing the epidemic wave that  
364 invaded the Durance River valley in 2008. To do so, we assessed the coverage rate of the raw  
365 sampling data (proportions of infected trees) based on their 95%-confidence intervals (Appendix  
366 S4.4, Figure 5). Over all sampling dates, the total coverage rate is high (~~0.75~~0.71), which indicates  
367 that the model indeed captures a large part of the strong variability of the data. By comparison,  
368 coverage rates given by models  $J_{\text{Exp}}$  and  $J_{\text{Gauss}}$  (~~0.69~~0.68 and 0.67, respectively) show a poorer fit  
369 to the data, especially for the first sampling date (Figures S6, S7) where the epidemic intensity is  
370 underestimated upstream and overestimated downstream.

## 371 5 Discussion

372 This study combines mechanistic and statistical modelling to jointly infer the demographic and dis-  
373 persal parameters underlying a biological invasion. A strength of the mechanistic model was to  
374 combine population growth with a large diversity of dispersal processes. The mechanistic model  
375 was coupled to a sound statistical model that considers different types of count data. These ob-  
376 servation laws consider that habitat suitability and disease perception can vary over the sampling  
377 domain. Simulations were designed to prove that the demographic model can be confidently selec-  
378 ted and its parameter values reliably inferred. Although the framework is generic, it was tuned to fit

379 the annual spread of the poplar rust fungus *M. larici-populina* along the Durance River valley. This  
380 valley channels every year the spread of an epidemic along a one-dimensional corridor of nearly  
381 200 km (Xhaard et al., 2012; Becheler et al., 2016). The monitoring we performed enables to build  
382 a comprehensive data set at a large spatial scale, which is mandatory to precisely infer the shape of  
383 the tail of dispersal kernels (Ferrandino, 1996; Kuparinen et al., 2007). A widely used alternative to  
384 the mechanistic-statistical approaches is to consider purely correlative approaches. However, the es-  
385 timated parameters defining the strength of the temporal and spatial dependencies (as estimated for  
386 example using R-INLA package approach, Rue et al., 2009) will not allow to distinguish between  
387 the different shapes of dispersal kernels, which was the main goal of our work.

## 388 **5.1 Estimation of the dispersal kernel of the poplar rust**

389 This study provides the first reliable estimation of the dispersal kernel of the poplar rust fungus.  
390 Dispersal kernels are firstly defined by their scale, which can be taken to correspond to the mean  
391 dispersal distance. The mean dispersal distance obtained from the best model is ~~2.01~~1.94 km with  
392 a 95% confidence interval ranging from ~~1.76 to 2.27~~1.78 to 2.12 km. A non-systematic literature  
393 review identified only eight studies reporting dispersal kernels for plant pathogens that used data  
394 gathered in experimental designs extending over regions bigger than 1 km (Fabre et al., 2021). The  
395 mean dispersal distances of the four fungal pathosystems listed by these authors are 213 m for the  
396 ascospores of *Mycosphaerella fijiensis* (Rieux et al., 2014), 490 m for the ascospores of *Lepto-*  
397 *sphaeria maculans* (Bousset et al., 2015), 860 m for *Podosphaera plantaginis* (Soubeyrand et al.,  
398 2009a) and from 1380 to 2560 m for *Hymenoscyphus fraxineus* (Grosdidier et al., 2018). Our estim-  
399 ates for poplar rust are in the same range as the one obtained at regional scale for *Hymenoscyphus*

400 *fraxineus*, the causal agent of Chalara ash dieback (Grosdidier et al., 2018).

401

402 Dispersal kernels can be further defined by their shape. We show that the spread of poplar  
403 rust is best described by a fat-tailed Exponential-power kernel. The thin-tailed kernels considered  
404 (Gaussian and exponential kernels) were clearly rejected by model selection. These results are in  
405 accordance with the high dispersal ability and the long-distance dispersal events evidenced in this  
406 species by population genetics analyses (Barrès et al., 2008; Becheler et al., 2016). Rust fungi are  
407 well-known to be wind dispersed over long distances (Brown and Hovmøller, 2002; Aylor, 2003).  
408 Recently, Severns et al. (2019) gathered experimental and simulation evidence that supports that  
409 wheat stripe rust spread supports theoretical scaling relationships from power law properties, an-  
410 other family of fat-tail dispersal kernel. In fact, many aeri-ally dispersed pathogens are likely to  
411 display frequent long-distance flights as soon as their propagules (spores, insect vectors) escape  
412 from plant canopy into turbulent air layer (Ferrandino, 1993; Pan et al., 2010). Accordingly, four  
413 of these eight studies listed by Fabre et al. (2021) lent support to fat-tailed kernels, including plant  
414 pathogens as diverse as viruses, fungi, and oomycetes.

415

## 416 **5.2 Effect of fat-tailed dispersal kernels on eco-evolutionary dynamics**

417 The dynamics produced by the mechanistic integro-differential models we use strongly depends  
418 on the tail of the dispersal kernel. Namely, when the equation is homogeneous (*i.e.* when the  
419 model parameters do not vary in space, leading to  $r(x) = r$ ), it is well known that for any thin-tailed  
420 dispersal kernel  $J$  such that  $\int_{\mathbb{R}} J(z) e^{\lambda|z|} dz < +\infty$  for some  $\lambda > 0$ , the dynamics of  $u(t, x)$  is well

421 explained using a particular solution called travelling wave. In this case, the invading front described  
422 by the solution  $u(t, x)$  moves at a constant speed (Aronson and Weinberger, 1978). By contrast, for a  
423 fat-tailed kernel, these particular solutions do not exist anymore, and the dynamic of  $u(t, x)$  describes  
424 an accelerated invasion process (Medlock and Kot, 2003; Garnier, 2011; Bouin et al., 2018). Here,  
425 we show that the dynamics of the poplar rust is better described as an accelerated invasion process  
426 rather than a front moving at a constant speed. Such accelerating wave at the epidemic front has  
427 been identified for several fungal plant pathogens dispersed by wind, including *Puccinia striiformis*  
428 and *Phytophthora infestans* the wheat stripe rust and the potato late blight, respectively (Mundt  
429 et al., 2009). However, it should be stated that fat-tailed kernels are not always associated with  
430 accelerated invasion processes. Indeed, fat-tailed kernels can be further distinguished depending on  
431 whether they are regularly varying (*e.g.* power law kernels) or rapidly varying (*e.g.* Exponential-  
432 power kernels) (Klein et al., 2006). Mathematically, it implies that power law kernels decrease  
433 even more slowly than any Exponential-power function. Biologically, fat-tailed Exponential-power  
434 kernels display rarer long-distance dispersal events than power law kernels. On the theoretical  
435 side, the kernel's properties subtly interact with demographic mechanisms such as Allee effects  
436 to possibly cancel the acceleration of invasion. With weak Allee effects (*i.e.* the growth rate is  
437 density dependent but still positive), no acceleration occurs with rapidly varying kernels whereas an  
438 acceleration could be observed for some regularly varying kernels, depending on the strength of the  
439 density dependence (Alfaro and Coville, 2017; Bouin et al., 2021). For strong Allee effects (*i.e.* a  
440 negative growth rate at low density), no acceleration can be observed for all possible kernels (Chen,  
441 1997). On the applied side, whether or not the epidemic wave is accelerating sharply impacts the  
442 control strategies of plant pathogens (Filipe et al., 2012; Ojiambo et al., 2015; Fabre et al., 2021).

### 443 **5.3 Confidence in the inference of the dispersal process**

444 The inference framework we developed is reasonably efficient in estimating the dispersal process  
445 with frequent long-distance dispersal events as generated by Exponential-power dispersal kernels.  
446 The numerical experiments clearly show that the lower the exponent parameter  $\tau$  of the Exponential-  
447 power kernel, the higher the confidence in its selection.

448 Conversely, the identification of the dispersal process is less accurate with thin-tail kernels.  
449 The requirement for improving the capacity to distinguish between thin-tail kernels may lie in the  
450 sampling scheme. Here, our sampling sites are regularly spaced, over a large sampling domain of  
451 200 km, which is better suited to monitor long-distance dispersal (Kuparinen et al., 2007). Sampling  
452 schemes with more frequent data in both time and space (or nested spatial sampling) might improve  
453 kernel identification.

454 We clearly observed that integro-differential models with Gaussian dispersal kernel on the one  
455 hand and reaction-diffusion equation on the other hand are well identified with our estimation pro-  
456 cedure when the time and space sampling is dense enough. This result may at first appear striking as  
457 a common belief tends to consider that diffusion amounts to a Gaussian dispersal kernel. However,  
458 these two models represent different movement processes (Othmer et al., 1988). In addition, clas-  
459 sical macroscopic diffusion, which is mainly based on Brownian motion (Othmer et al., 1988), often  
460 ignores the inherent variability among individuals' capacity of movements and as a consequence  
461 does not accurately describe the dispersal at the population scale (Hapca et al., 2009). While it is  
462 reasonable to assume that a single individual disperses via Brownian motion, this assumption hardly  
463 extends to all individuals in the population. Accordingly, we believe that integro-differential mod-  
464 els are better suited to take into account inter-individual behaviour as the dispersal kernel explicitly



465 models the redistribution of individuals.

## 466 **5.4 Robustness and portability of the method**

467 A strength of the approach proposed is the detailed description of the observation laws in the statistical model. The derivation of their probability density functions allows to obtain an analytical  
468 expression of the likelihood function. Model inference was however not straightforward due to  
469 local optimum issues. In order to achieve satisfying computational efficiency, we developed an *ad hoc*  
470 hybrid strategy initiated from 20 initial values and combining the two classical Nelder-Mead  
471 and Nlminb optimisation algorithms. However, the framework of hierarchical statistical models  
472 (Cressie et al., 2009), whose inference is often facilitated by Bayesian approaches, could likely be  
473 mobilised to improve model fit. In particular, although the coverage rate of the tree sampling was  
474 correct, it could be further improved by relaxing some hypotheses. The orange-coloured uredinia  
475 being easily seen on green leaves, we assumed that the persons in charge of the sampling perfectly  
476 detect the disease as soon as a single uredinia is present on a leaf. However, even in this context,  
477 observation errors are likely present in our dataset as in any large spatio-temporal study. The latent  
478 variables used in hierarchical models are best suited to handle the fact that a tree observed to be  
479 healthy can actually be infected. False detection of infection could also be taken into account. This  
480 could make sense as a sister species, *M. alli-populina*, not easily discernible from *M. larici-populina*  
481 in the field, can also infect poplar leaves. This species can predominate locally in the downstream  
482 part of the Durance River valley. This could have led to over-estimate the disease severity at some  
483 locations. Yet, all infected leaves from twigs were collected and minutely inspected in the lab under  
484 a Stereo Microscope (25 magnification) to check for species identification.  
485

486 More generally, the statistical part of the mechanistic-statistical approaches developed could be  
487 transposed to a wide range of organisms and sampling types. Sharing the sampling effort between  
488 raw and refined samples improves the estimations. The two distinct types of sampling (sampling  
489 of random leaves in trees, and of leaves grouped within twigs) apply to a wide range of species,  
490 which local distribution is aggregated into patches randomly scattered across a study site. Any  
491 biological study with two such distinct sampling types (as described in Figure 1) would fit the  
492 proposed statistical model. One can for example scale up the sampling by considering the plant  
493 (instead of the leaf) as the basic unit. Moreover, the framework naturally copes with the diversity  
494 of sampling schemes on the ground such as the absence of one sample type for all or part of the  
495 sampled sites and dates. Finally, we used the first sampling date to estimate independently the initial  
496 population densities  $u(0, x)$  that were then fixed among all simulated epidemics. Future works could  
497 as well jointly estimate  $u(0, x)$  as part of  $\theta$ .

498 The mechanistic part of the model could also handle a wider diversity of hypotheses. First, the  
499 model can be adapted to take into account a wider range of dispersal kernels, such as regularly  
500 varying kernels (see above). Second, the model can also easily be adapted to take into account para-  
501 meter heterogeneity in time and space of its parameters. Similarly, one may easily assume that the  
502 growth rate depends on daily meteorological variables. Finally, we ignore the influence of the local  
503 fluctuations of the population size on the macro-scale density of the population when stochastic  
504 fluctuations can influence epidemic dynamics (Rohani et al., 2002). Here, we neglect this influence  
505 by considering that the average population size is relevant when habitat units are aggregated. Re-  
506 laxing this hypothesis could be achieved by incorporating stochastic integro-differential equations.  
507 The inference of such models is currently a front of research.

## 508 **5.5 Future directions**

509 As biological invasions are regularly observed retrospectively, carrying out spatio-temporal moni-  
510 oring is often highly difficult, when possible. A small number of longitudinal temporal data makes  
511 model inference very difficult, in particular for its propensity to properly disentangle the effect  
512 of growth rate and dispersal. Incorporating genetic data into the framework proposed here is a  
513 challenge that must be met to get around this problem. Indeed, colonisation and demographic ef-  
514 fects such as Allee effect generate their own specific genetic signatures (Dennis, 1989; Lewis and  
515 Kareiva, 1993; Miller et al., 2020). Similarly, genetic data could help to identify the dispersal kernel  
516 underlying the invasion process, as the population will exhibit an erosion of its neutral diversity with  
517 a thin-tailed kernel (Edmonds et al., 2004; Hallatschek et al., 2007). Conversely, genetic diversity  
518 can be preserved all along the invasion front with a fat-tailed kernel, because of the long-distance  
519 dispersal of individuals from the back of the front, where genetic diversity is conserved (Fayard  
520 et al., 2009; Bonnefon et al., 2014).

## 521 **Acknowledgements**

522 We warmly thank all the collectors who participated in the monitoring of the poplar rust disease  
523 spread along the Durance River valley: Audrey Andanson, Béranger Bertin, Olivier Caël, Bénédicte  
524 Fabre, Christine Gehin, Claude Husson, Benoît Marçais, and Agathe Vialle. We also thank Benoît  
525 Marçais for fruitful discussions on disease monitoring, Bénédicte Fabre for the calculus of the dens-  
526 ity in uredinia on a poplar leaf, and Fabrice Elegbede for advices on statistical analyses. This work  
527 was supported by grants from the French National Research Agency (ANR-09-BLAN-0145, EMILE  
528 project; ANR-18-CE32-0001, CLONIX2D project; ANR-14-CE25-0013, project NONLOCAL,

529 ANR-11-LABX-0002-01, Cluster of Excellence ARBRE; 20-PCPA-0002, BEYOND project). Con-  
530 stance Xhaard was supported by a PhD fellowship from the French Ministry of Education and  
531 Research (MESR) and by Postdoc fellowship from the French National Research Agency (ANR-  
532 09-BLAN-0145, EMILE project) . Méline Saubin was supported by a PhD fellowship from INRAE  
533 and the French National Research Agency (ANR-18-CE32-0001, CLONIX2D project).

## 534 **Author contributions**

535 Constance Xhaard, Pascal Frey, and Fabien Halkett supervised the disease monitoring. Jérôme  
536 Coville, Frédéric Fabre, Fabien Halkett, and Samuel Soubeyrand conceived and designed the study.  
537 Jérôme Coville provided a mathematical expertise on modelling long-range dispersal as well as  
538 codes of simulation for the mechanistic models. Samuel Soubeyrand established the observation  
539 laws. Frédéric Fabre supervised the statistical analyses. Constance Xhaard and Fabien Halkett did  
540 preliminary analyses. Méline Saubin updated the code and did the statistical analyses. Jérôme  
541 Coville, Frédéric Fabre, Fabien Halkett, Méline Saubin, and Samuel Soubeyrand contributed to the  
542 writing of the manuscript. All authors read and approved the manuscript.

## 543 **Competing interests**

544 The authors declare that they comply with the PCI rule of having no financial conflicts of interest in  
545 relation to the content of the article.

## 546 **Data accessibility**

547 R and C++ scripts for model simulations and statistical analyses, as well as count data for the bio-  
548 logical application, are available on a public Zenodo repository (DOI:10.5281/zenodo.7906841),  
549 extracted from a public GitLab repository: [https://gitlab.com/saubin.meline/mechanistic-statistical-](https://gitlab.com/saubin.meline/mechanistic-statistical-model)  
550 [model](https://gitlab.com/saubin.meline/mechanistic-statistical-model).

## 551 **References**

- 552 Alfaro, M. and Coville, J. (2017). Propagation phenomena in monostable integro-differential equa-  
553 tions: Acceleration or not? *Journal of Differential Equations*, 263(9):5727–5758.
- 554 Aronson, D. G. and Weinberger, H. F. (1978). Multidimensional nonlinear diffusion arising in  
555 population genetics. *Advances in Mathematics*, 30(1):33–76.
- 556 Aylor, D. E. (2003). Spread of plant disease on a continental scale: Role of aerial dispersal of  
557 pathogens. *Ecology*, 84(8):1989–1997.
- 558 Barrès, B., Halkett, F., Dutech, C., Andrieux, A., Pinon, J., and Frey, P. (2008). Genetic structure of  
559 the poplar rust fungus *Melampsora larici-populina*: Evidence for isolation by distance in Europe  
560 and recent founder effects overseas. *Infection, Genetics and Evolution*, 8(5):577–587.
- 561 Becheler, R., Xhaard, C., Klein, E., Hayden, K. J., Frey, P., De Mita, S., and Halkett, F. (2016).  
562 Genetic signatures of a range expansion in natura: when clones play leapfrog. *Ecology and*  
563 *Evolution*, 6(18):6625–6632.

- 564 Berliner, L. M. (2003). Physical-statistical modeling in geophysics. *Journal of Geophysical Re-*  
565 *search*, 108(24):8776.
- 566 Bialozyt, R., Ziegenhagen, B., and Petit, R. J. (2006). Contrasting effects of long distance seed  
567 dispersal on genetic diversity during range expansion. *Journal of Evolutionary Biology*, 19(1):12–  
568 20.
- 569 Bonnefon, O., Coville, J., Garnier, J., Hamel, F., and Roques, L. (2014). The spatio-temporal  
570 dynamics of neutral genetic diversity. *Ecological Complexity*, 20:282–292.
- 571 Bouin, E., Coville, J., and Legendre, G. (2021). Sharp exponent of acceleration in general nonlocal  
572 equations with a weak Allee effect. *arXiv*, pages 1–45.
- 573 Bouin, E., Garnier, J., Henderson, C., and Patout, F. (2018). Thin front limit of an integro-  
574 differential Fisher-KPP equation with fat-tailed kernels. *SIAM Journal on Mathematical Analysis*,  
575 50(3):3365–3394.
- 576 Bourgeois, A., Gaba, S., Munier-Jolain, N., Borgy, B., Monestiez, P., and Soubeyrand, S. (2012).  
577 Inferring weed spatial distribution from multi-type data. *Ecological Modelling*, 226:92–98.
- 578 Bousset, L., Jumel, S., Garreta, V., Picault, H., and Soubeyrand, S. (2015). Transmission of *Lepto-*  
579 *sphaeria maculans* from a cropping season to the following one. *Annals of Applied Biology*,  
580 166(3):530–543.
- 581 Brown, J. K. M. and Hovmøller, M. S. (2002). Aerial dispersal of pathogens on the global and  
582 continental scales and its impact on plant disease. *Science*, 297:537–541.

- 583 Chagneau, P., Mortier, F., Picard, N., and Bacro, J. (2011). A hierarchical Bayesian model for  
584 spatial prediction of multivariate non-Gaussian random fields. *Biometrics*, 67(1):97–105.
- 585 Chen, X. (1997). Existence, uniqueness, and asymptotic stability of traveling waves in nonlocal  
586 evolution equations. *Advances in Differential Equations*, 2(1):125–160.
- 587 Clark, J. S., Lewis, M., and Horvath, L. (2001). Invasion by extremes: Population spread with  
588 variation in dispersal and reproduction. *American Naturalist*, 157(5):537–554.
- 589 Clobert, J., Ims, R. A., and Rousset, F. (2004). Causes, mechanisms and consequences of dispersal.  
590 In *Ecology, genetics and evolution of metapopulations*, pages 307–335. Elsevier.
- 591 Cressie, N., Calder, C. A., Clark, J. S., Ver Hoef, J. M., and Wikle, C. K. (2009). Accounting  
592 for uncertainty in ecological analysis: The strengths and limitations of hierarchical statistical  
593 modeling. *Ecological Applications*, 19(3):553–570.
- 594 Dennis, B. (1989). Allee effects: Population growth, critical density, and the chance of extinction.  
595 *Natural Resource Modeling*, 3(4):481–538.
- 596 Dybiec, B., Kleczkowski, A., and Gilligan, C. A. (2009). Modelling control of epidemics spreading  
597 by long-range interactions. *Journal of the Royal Society Interface*, 6(39):941–950.
- 598 Edmonds, C. A., Lillie, A. S., and Cavalli-Sforza, L. L. (2004). Mutations arising in the wave front  
599 of an expanding population. *Proceedings of the National Academy of Sciences*, 101(4):975–979.
- 600 Fabre, F., Coville, J., and Cunniffe, N. J. (2021). Optimising reactive disease management using  
601 spatially explicit models at the landscape scale. In Scott, P. R., Strange, R. N., Korsten, L., and

602 Gullino, M. L., editors, *Plant disease and food security in the 21st century*, pages 47–72. Springer  
603 International Publishing.

604 Fayard, J., Klein, E., and Lefèvre, F. (2009). Long distance dispersal and the fate of a gene from  
605 the colonization front. *Journal of Evolutionary Biology*, 22(11):2171–2182.

606 Ferrandino, F. J. (1993). Dispersive epidemic waves: I. Focus expansion within a linear planting.  
607 *Phytopathology*, 83(8):795.

608 Ferrandino, F. J. (1996). Length scale of disease spread: Fact or artifact of experimental geometry.  
609 *Phytopathology*, 86:806–811.

610 Fife, P. C. (1996). An integrodifferential analog of semilinear parabolic PDEs. In *Partial differential*  
611 *equations and applications*, volume 177 of *Lecture Notes in Pure and Appl. Math.*, pages 137–  
612 145. Dekker, New York.

613 Filipe, J. A. N., Cobb, R. C., Meentemeyer, R. K., Lee, C. A., Valachovic, Y. S., Cook, A. R.,  
614 Rizzo, D. M., and Gilligan, C. A. (2012). Landscape epidemiology and control of pathogens  
615 with cryptic and long-distance dispersal: Sudden Oak death in northern Californian forests. *PLoS*  
616 *Computational Biology*, 8(1):e1002328.

617 Gandon, S. and Michalakis, Y. (2002). Local adaptation, evolutionary potential and host para-  
618 site coevolution: Interactions between migration, mutation, population size and generation time.  
619 *Journal of Evolutionary Biology*, 15(3):451–462.

620 Garnier, J. (2011). Accelerating solutions in integro-differential equations. *SIAM Journal on Math-*  
621 *ematical Analysis*, 43:1955–1974.



- 622 Georgescu, V., Desassis, N., Soubeyrand, S., Kretzschmar, A., and Senoussi, R. (2014). An auto-  
623 mated MCEM algorithm for hierarchical models with multivariate and multitype response vari-  
624 ables. *Communications in Statistics - Theory and Methods*, 43(17):3698–3719.
- 625 Gotway, C. A. and Young, L. J. (2002). Combining incompatible spatial data. *Journal of the*  
626 *American Statistical Association*, 97(458):632–648.
- 627 Grosdidier, M., Ioos, R., Husson, C., Cael, O., Scordia, T., and Marçais, B. (2018). Tracking the  
628 invasion: dispersal of *Hymenoscyphus fraxineus* airborne inoculum at different scales. *FEMS*  
629 *Microbiology Ecology*, 94(5):1–11.
- 630 Hallatschek, O. and Fisher, D. S. (2014). Acceleration of evolutionary spread by long-range dis-  
631 persal. *Proceedings of the National Academy of Sciences*, 111(46):E4911–E4919.
- 632 Hallatschek, O., Hersen, P., Ramanathan, S., and Nelson, D. R. (2007). Genetic drift at expand-  
633 ing frontiers promotes gene segregation. *Proceedings of the National Academy of Sciences*,  
634 104(50):19926–19930.
- 635 Hapca, S., Crawford, J. W., and Young, I. M. (2009). Anomalous diffusion of heterogeneous pop-  
636 ulations characterized by normal diffusion at the individual level. *Journal of the Royal Society*  
637 *Interface*, 6(30):111–122.
- 638 Hefley, T. J., Hooten, M. B., Russell, R. E., Walsh, D. P., and Powell, J. A. (2017). When mechanism  
639 matters: Bayesian forecasting using models of ecological diffusion. *Ecology Letters*, 20(5):640–  
640 650.
- 641 Hutson, V., Martinez, S., Mischaikow, K., and Vickers, G. T. (2003). The evolution of dispersal.  
642 *Journal of Mathematical Biology*, 47(6):483–517.

- 643 Ibrahim, K. M., Nichols, R. A., and Hewitt, G. M. (1996). Spatial patterns of genetic variation  
644 generated by different forms of dispersal during range expansion. *Heredity*, 77:282–291.
- 645 Klein, E., Lavigne, C., Picault, H., Renard, M., and Gouyon, P. H. (2006). Pollen dispersal of  
646 oilseed rape: Estimation of the dispersal function and effects of field dimension. *Journal of*  
647 *Applied Ecology*, 43(1):141–151.
- 648 Kolmogorov, A. N., Petrovsky, I. G., and Piskunov, N. S. (1937). Étude de l'équation de la diffusion  
649 avec croissance de la quantité de matière et son application à un problème biologique. *Bulletin*  
650 *Université d'État à Moscow (Bjul. Moskowskogo Gos. Univ)*, pages 1–26.
- 651 Kot, M., Lewis, M. A., and van den Driessche, P. (1996). Dispersal data and the spread of invading  
652 organisms. *Ecology*, 77(7):2027–2042.
- 653 Kuparinen, A., Snäll, T., Vänskä, S., and O'Hara, R. B. (2007). The role of model selection in  
654 describing stochastic ecological processes. *Oikos*, 116(6):966–974.
- 655 Lewis, M. A. and Kareiva, P. (1993). Allee dynamics and the spread of invading organisms. *Theor-*  
656 *etical Population Biology*, 42:141–158.
- 657 Louvrier, J., Papaïx, J., Duchamp, C., and Gimenez, O. (2020). A mechanistic-statistical spe-  
658 cies distribution model to explain and forecast wolf (*Canis lupus*) colonization in South-Eastern  
659 France. *Spatial Statistics*, 36:100428.
- 660 Macdonald, D. W. and Johnson, D. D. P. (2001). Dispersal in theory and practice: consequences for  
661 conservation biology. In Clober, T. J., Danchin, E., Dhondt, A. A., and Nichols, J. D., editors,  
662 *Dispersal*, chapter 25, pages 361–374. Oxford University Press, Oxford, UK.

663 Medlock, J. and Kot, M. (2003). Spreading disease: Integro-differential equations old and new.  
664 *Mathematical Biosciences*, 184(2):201–222.

665 Miller, T. E. X., Angert, A. L., Brown, C. D., Lee-Yaw, J. A., Lewis, M., Lutscher, F., Marculis,  
666 N. G., Melbourne, B. A., Shaw, A. K., Szcs, M., Tabares, O., Usui, T., Weiss-Lehman, C., and  
667 Williams, J. L. (2020). Eco-evolutionary dynamics of range expansion. *Ecology*, 101(10):1–14.

668 Mollison, D. (1977). Spatial contact models for ecological and epidemic spread. *Journal of the*  
669 *Royal Statistical Society: Series B (Methodological)*, 39:283–326.

670 Mundt, C. C., Sackett, K. E., Wallace, L. D., Cowger, C., and Dudley, J. P. (2009). Long-distance  
671 dispersal and accelerating waves of disease: Empirical relationships. *American Naturalist*,  
672 173(4):456–466.

673 Murray, J. D. (2002). *Mathematical Biology*, volume 17. Springer-Verlag, third edition.

674 Nathan, R. (2001). The challenges of studying dispersal. *Trends in Ecology and Evolution*,  
675 16(9):481–483.

676 Nathan, R., Klein, E., Robledo-Arnuncio, J. J., and Revilla, E. (2012). 15 - Dispersal kernels:  
677 Review. In Clobert, J., Baguette, M., Benton, T. G., and Bullock, J. M., editors, *Dispersal*  
678 *ecology and evolution*, pages 186–210. Oxford.

679 Nembot Fomba, C. G., Ten Hoopen, G. M., Soubeyrand, S., Roques, L., Ambang, Z., and Takam  
680 Soh, P. (2021). Parameter estimation in a PDE model for the spatial spread of cocoa black pod  
681 disease. *Bulletin of Mathematical Biology*, 83:1–28.

- 682 Nichols, R. A. and Hewitt, G. M. (1994). The genetic consequences of long distance dispersal  
683 during colonization. *Heredity*, 72:312–317.
- 684 Ojiambo, P. S., Gent, D. H., Quesada-Ocampo, L. M., Hausbeck, M. K., and Holmes, G. J. (2015).  
685 Epidemiology and population biology of *Pseudoperonospora cubensis* : A model system for  
686 management of downy mildews. *Annual Review of Phytopathology*, 53(1):223–246.
- 687 Okubo, A. and Levin, S. A. (2002). *Diffusion and Ecological Problems – Modern Perspectives*.  
688 Second edition, Springer-Verlag, New York.
- 689 Othmer, H. G., Dunbar, S. R., and Alt, W. (1988). Models of dispersal in biological systems.  
690 *Journal of Mathematical Biology*, 26(3):263–298.
- 691 Pan, Z., Li, X., Yang, X. B., Andrade, D., Xue, L., and McKinney, N. (2010). Prediction of  
692 plant diseases through modelling and monitoring airborne pathogen dispersal. *CAB Reviews:*  
693 *Perspectives in Agriculture, Veterinary Science, Nutrition and Natural Resources*, 5(018).
- 694 Papaïx, J., Soubeyrand, S., Bonnefon, O., Walker, E., Louvrier, J., Klein, E., and Roques, L. (2022).  
695 Inferring mechanistic models in spatial ecology using a mechanistic-statistical approach. In *Stat-*  
696 *istical Approaches for Hidden Variables in Ecology*, pages 69–95. Wiley.
- 697 Petit, R. J. (2004). Biological invasions at the gene level. *Diversity and Distributions*, 10(3):159–  
698 165.
- 699 Petit, R. J. (2011). Early insights into the genetic consequences of range expansions. *Heredity*,  
700 106:203–204.
- 701 Rieux, A., Soubeyrand, S., Bonnot, F., Klein, E. K., Ngando, J. E., Mehl, A., Ravigne, V., Carlier,

702 J., and Bellaire, L. (2014). Long-distance wind-dispersal of spores in a fungal plant patho-  
703 gen: Estimation of anisotropic dispersal kernels from an extensive field experiment. *PLoS One*,  
704 9(8):e103225.

705 Rohani, P., Keeling, M. J., and Grenfell, B. T. (2002). The interplay between determinism and  
706 stochasticity in childhood diseases. *The American Naturalist*, 159:469–481.

707 Roques, L., Soubeyrand, S., and Rousselet, J. (2011). A statistical-reaction-diffusion approach for  
708 analyzing expansion processes. *Journal of Theoretical Biology*, 274(1):43–51.

709 Rue, H., Martino, S., and Chopin, N. (2009). Approximate Bayesian inference for latent Gaus-  
710 sian models by using integrated nested Laplace approximations. *Journal of the Royal Statistical*  
711 *Society: Series B (Statistical Methodology)*, 71(2):319–392.

712 Severns, P. M., Sackett, K. E., Farber, D. H., and Mundt, C. C. (2019). Consequences of  
713 long-distance dispersal for epidemic spread: Patterns, scaling, and mitigation. *Plant Disease*,  
714 103(2):177–191.

715 Shigesada, N. and Kawasaki, K. (1997). *Biological invasions: Theory and practice*. Oxford Uni-  
716 versity Press, UK.

717 Soubeyrand, S., de Jerphanion, P., Martin, O., Saussac, M., Manceau, C., Hendriks, P., and Lannou,  
718 C. (2018). Inferring pathogen dynamics from temporal count data: the emergence of *Xylella*  
719 *fastidiosa* in France is probably not recent. *New Phytologist*, 219:824–836.

720 Soubeyrand, S., Laine, A. L., Hanski, I., and Penttinen, A. (2009a). Spatio-temporal structure of  
721 host-pathogen interactions in a metapopulation. *The American Naturalist*, 174(3):308–320.

- 722 Soubeyrand, S., Neuvonen, S., and Penttinen, A. (2009b). Mechanical-statistical modeling in eco-  
723     logy: From outbreak detections to pest dynamics. *Bulletin of Mathematical Biology*, 71:318–338.
- 724 Soubeyrand, S. and Roques, L. (2014). Parameter estimation for reaction-diffusion models of bio-  
725     logical invasions. *Population Ecology*, 56(2):427–434.
- 726 Soubeyrand, S., Sache, I., Hamelin, F., and Klein, E. K. (2015). Evolution of dispersal in asexual  
727     populations: to be independent, clumped or grouped? *Evolutionary Ecology*, 29:947–963.
- 728 Szymańska, Z., Skrzeczkowski, J., Miasojedow, B., and Gwiazda, P. (2021). Bayesian inference of  
729     a non-local proliferation model. *Royal Society Open Science*, 8(11).
- 730 Wikle, C. K. (2003a). Hierarchical Bayesian models for predicting the spread of ecological pro-  
731     cesses. *Ecology*, 84(6):1382–1394.
- 732 Wikle, C. K. (2003b). Hierarchical models in environmental science. *International Statistical*  
733     *Review*, 71(2):181–199.
- 734 Xhaard, C., Barrès, B., Andrieux, A., Bousset, L., Halkett, F., and Frey, P. (2012). Disentangling the  
735     genetic origins of a plant pathogen during disease spread using an original molecular epidemi-  
736     ology approach. *Molecular Ecology*, 21(10):2383–2398.

Table 1: Model practical identifiability. Numbers indicate the coefficient of correlation between the true and estimated parameter values for the four models corresponding to the four dispersal processes ( $J_{\text{Exp}}$ ,  $J_{\text{Gauss}}$ ,  $J_{\text{ExpP}}$  and R.D.) from ~~100~~-160 replicates. High correlation between true and estimated parameters indicates a good practical identifiability. The standard deviations of the coefficients of correlation, estimated with a bootstrapping method, are indicated in brackets. Correlation coefficients and standard deviations are given for natural scale for parameter  $\omega$ , and logarithm scales for parameters  $r_{\text{dw}}$ ,  $\gamma$ ,  $\lambda$ ,  $\tau$ , and  $\sigma^2$ .

Parameter	Description	$J_{\text{Exp}}$	$J_{\text{Gauss}}$	$J_{\text{ExpP}}$
$r_{\text{dw}}$	Growth rate downstream	<del>0.99</del> ( $1 \cdot 10^{-3}$ ) <u>0.997 (0.001)</u>	<del>0.99</del> ( $1 \cdot 10^{-3}$ ) <u>0.997 (0.001)</u>	<del>0.99</del> ( $2 \cdot 10^{-3}$ ) <u>0.997 (0.001)</u>
$\omega$	Growth rate modulator	<del>0.99</del> ( $< 10^{-3}$ ) <u>0.997 (0.001)</u>	<del>0.99</del> ( $< 10^{-3}$ ) <u>0.992 (0.003)</u>	<del>0.99</del> ( $1 \cdot 10^{-3}$ ) <u>0.997 (0.001)</u>
$\lambda$	Mean dispersal distance	<del>0.99</del> ( $5 \cdot 10^{-3}$ ) <u>0.983 (0.007)</u>	<del>0.98</del> ( $8 \cdot 10^{-3}$ ) <u>0.993 (0.004)</u>	<del>0.99</del> ( $1 \cdot 10^{-3}$ ) <u>0.997 (0.001)</u>
$\tau$	Kernel exponent	NA	NA	<del>0.95</del> ( $1 \cdot 10^{-3}$ ) <u>0.997 (0.001)</u>
$\gamma$	Tree perception	<del>0.85</del> ( $4 \cdot 10^{-2}$ ) <u>0.969 (0.006)</u>	<del>0.83</del> ( $4 \cdot 10^{-2}$ ) <u>0.966 (0.006)</u>	<del>0.83</del> ( $5 \cdot 10^{-2}$ ) <u>0.966 (0.006)</u>
$\sigma^2$	Variance in leaf suitability	<del>0.99</del> ( $1 \cdot 10^{-3}$ ) <u>0.996 (0.001)</u>	<del>0.99</del> ( $< 10^{-3}$ ) <u>0.997 (0.001)</u>	<del>0.99</del> ( $< 10^{-3}$ ) <u>0.997 (0.001)</u>

Table 2: Efficiency of model selection using Akaike information criterion (AIC). The four first columns indicate the proportion of cases, among ~~50~~60 replicates, where each tested model was selected using AIC, given that data sets were generated under a particular model (*i.e.* true model). Column  $dAIC_{\text{true}}$  (*resp.*  $dAIC_{\text{wrong}}$ ) indicates the mean difference between the AIC of the model selected when the model selected is the true one (*resp.* when the model selected is not the true model) and the second best model (*resp.* being the true model or not).

True Model	Selected Model				$dAIC_{\text{true}}$	$dAIC_{\text{wrong}}$
	$J_{\text{Exp}}$	$J_{\text{Gauss}}$	$J_{\text{ExpP}}$	R.D.		
$J_{\text{Exp}}$	<del>0.62</del> <u>0.50</u>	<del>0.22</del> <u>0.32</u>	<del>0.06</del> <u>0.05</u>	<del>0.10</del> <u>0.13</u>	<del>0.84</del> <u>0.90</u>	<del>0.74</del> <u>1.10</u>
$J_{\text{Gauss}}$	<del>0.34</del> <u>0.25</u>	<del>0.26</del> <u>0.45</u>	<del>0.00</del> <u>0.02</u>	<del>0.40</del> <u>0.28</u>	<del>1.08</del> <u>1.30</u>	<del>0.55</del> <u>0.67</u>
$J_{\text{ExpP}}$	<del>0.20</del> <u>0.17</u>	<del>0.04</del> <u>0.05</u>	<del>0.70</del> <u>0.78</u>	<del>0.06</del> <u>0</u>	<del>89.62</del> <u>217.50</u>	<del>0.38</del> <u>0.76</u>
R.D.	<del>0.22</del> <u>0.22</u>	0.18	<del>0.24</del> <u>0</u>	<del>0.00</del> <u>0.60</u>	<del>0.58</del> <u>2.37</u>	<del>0.71</del> <u>0.23</u> <u>0.33</u>



Table 3: Model selection for the epidemic of poplar rust along the Durance River valley. The Akaike information criteria are indicated for each model fitted to the real data set. The model best supported by the data is indicated in bold.  $AIC_{\text{median}}$  and  $AIC_{\text{sd}}$  represent the median and standard deviation among the AIC obtained from five initial parameter values.

Dispersal	$AIC_{\text{median}}$	$AIC_{\text{sd}}$
$J_{\text{Exp}}$	<del>5476</del> <u>5461</u>	<del>0.68</del> <u>5.81</u>
$J_{\text{Gauss}}$	<del>5510</del> <u>5493</u>	<del>1.03</del> <u>0.15</u>
$J_{\text{ExpP}}$	<b><del>5179</del><u>5163</u></b>	<b><del>1.32</del><u>0.01</u></b>
R.D.	<del>6303</del> <u>6190</u>	<del>655.60</del> <u>0.03</u>

Table 4: Statistical summary of the inference of the parameters for the model best supported by the real data set  $J_{\text{Exp}}$ . We used the vector of parameters  $\theta$  giving the lowest AIC value in the previous model selection procedure as initial parameter values of the R function `mle2`, to obtain maximum likelihood estimates of the vector of parameters  $\hat{\theta}$  and of its matrix of variance-covariance  $\hat{\Sigma}$ . Summary statistics were derived from 1,000 random draws from the multivariate normal distribution with parameters  $\hat{\theta}$  and  $\hat{\Sigma}$  (see Appendix S4.3). Columns Estimate,  $q - 2.5\%$  and  $q - 97.5\%$  represent the estimated value of each parameter and the quantiles 2.5% and 97.5%, respectively.

Parameter	Description	$q - 2.5\%$	Estimate	$q - 97.5\%$
$r_{\text{up}}$	Growth rate upstream	<del>0.0312</del> <u>0.0786</u>	<del>0.0844</del> <u>0.0853</u>	<del>0.191</del> <u>0.0897</u>
$r_{\text{dw}}$	Growth rate downstream	<del>0.0114</del> <u>0.0143</u>	<del>0.0203</del> <u>0.0230</u>	<del>0.0289</del> <u>0.0311</u>
$\lambda$	Mean dispersal distance	<del>1.76</del> <u>1.78</u>	<del>2.01</del> <u>1.94</u>	<del>2.03</del> <u>2.12</u>
$\tau$	Kernel exponent	<del>0.220</del> <u>0.226</u>	<del>0.242</del> <u>0.243</u>	<del>0.263</del> <u>0.260</u>
$\gamma$	Tree perception	<del>3.21</del> <u>3.49</u>	<del>5.21</del> <u>4.82</u>	<del>6.77</del> <u>6.11</u>
$\sigma^2$	Variance in leaf suitability	<del>0.987</del> <u>1.23</u>	<del>1.09</del> <u>1.29</u>	<del>1.21</del> <u>1.36</u>

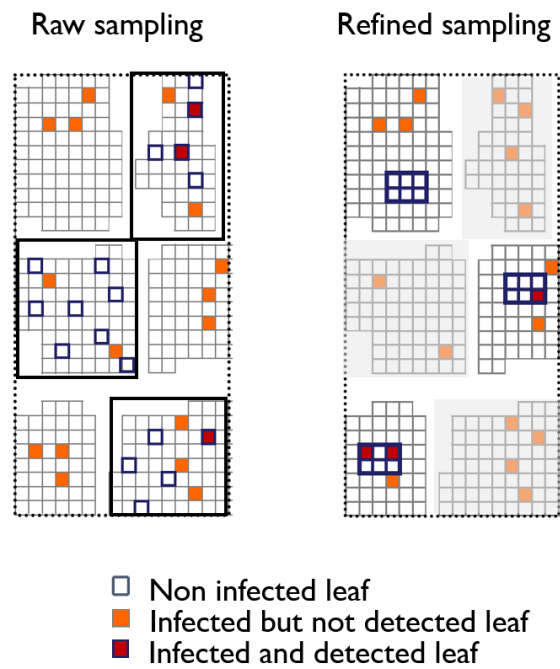


Figure 1: Two-stage sampling on a sampling site, with one systematic raw sampling (on the left) and one optional refined sampling (on the right). Each square represent a leaf, which can be non infected, infected but not detected, or infected and detected. Each group of spatially grouped leaves represent a tree. Each tree already observed during the raw sampling are not available (and thus represented in grey) for the refined sampling, where connected leaves in twigs are observed.

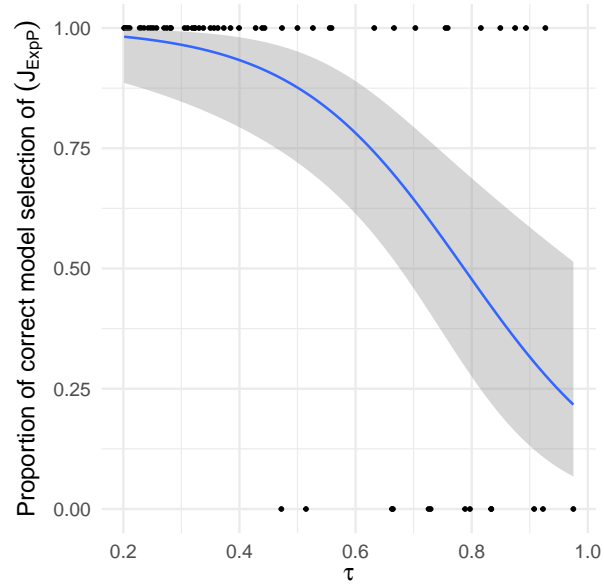


Figure 2: Logistic regression of the proportion of correct model selection of dispersal  $J_{ExpP}$  as a function of  $\tau$ . Dots represent the values of  $\tau$  used for the ~~50~~60 replicates of simulated dispersal model  $J_{ExpP}$ , and the estimated dispersal model (1 for a correct model selection of  $J_{ExpP}$  and 0 for a wrong model selection). The blue line corresponds to the predicted value of the proportion of correct model selection  $J_{ExpP}$  as a function of  $\tau$ , and the grey area corresponds to the confidence envelope at 95%.

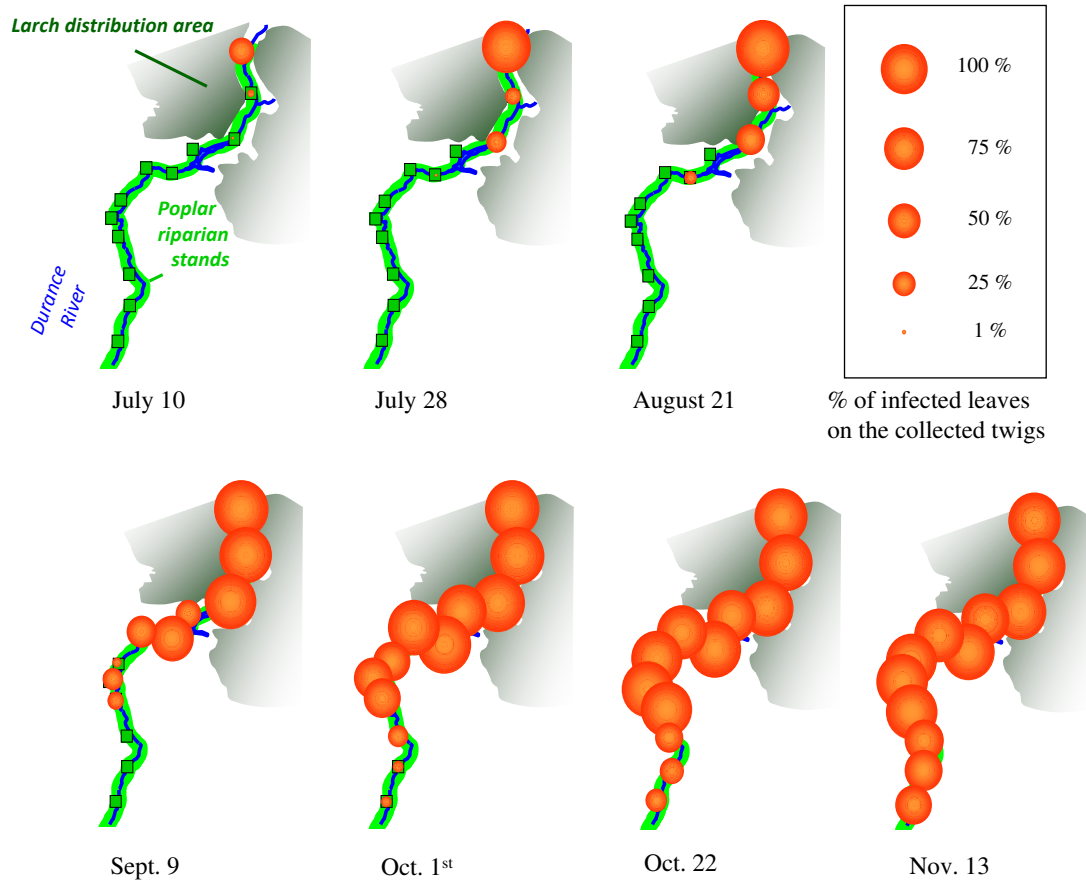


Figure 3: Poplar rust epidemic wave along the Durance River valley in 2008. The larch distribution area is represented in dark green, wild poplar riparian stands in pale green. The 12 study sites are represented by the green squares. Orange dots describe the evolution of the poplar rust epidemic through time (7 rounds of disease notation) and space (12 studied sites). Dot size is proportional to rust disease incidence assessed from the refined sampling.

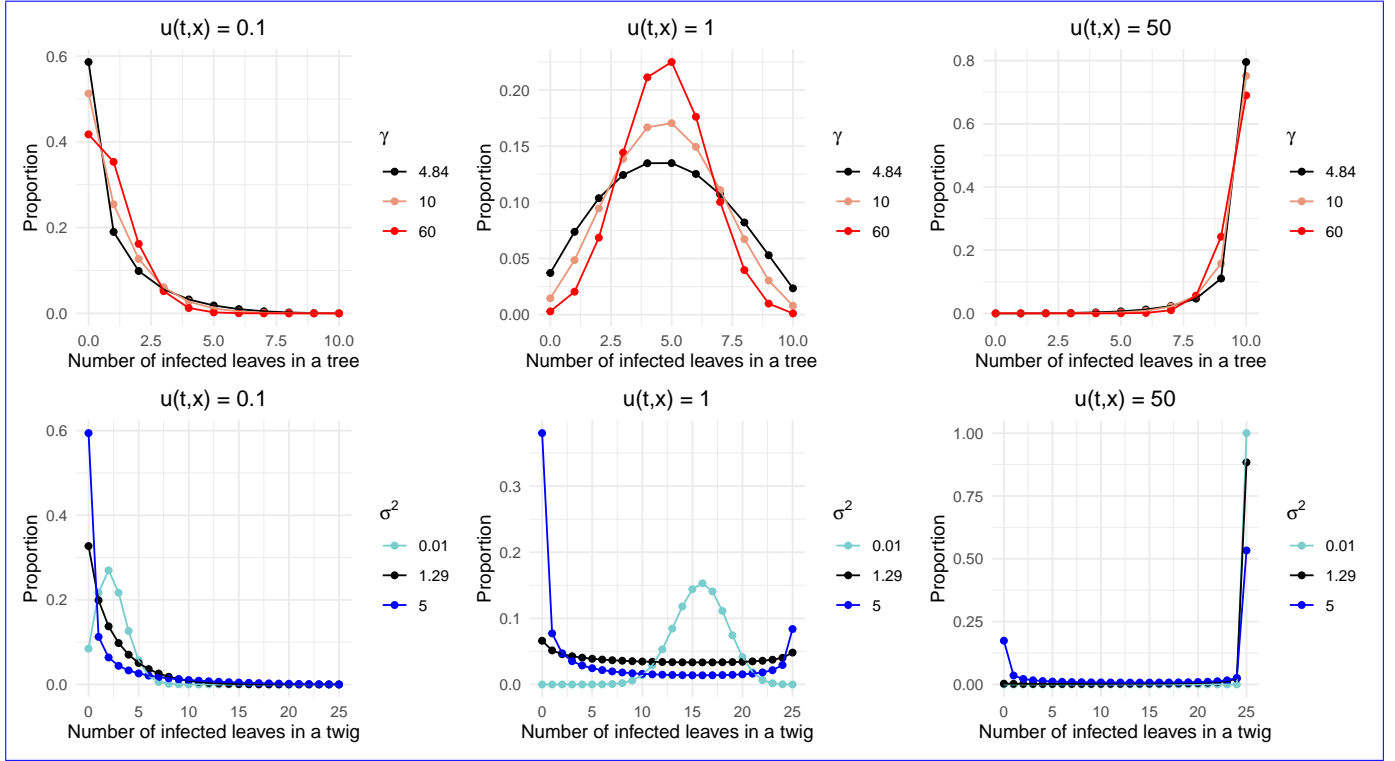


Figure 4: Distributions of the number of infected leaves in a tree and of the number of infected leaves in a twig, for increasing densities of infection  $u(t,x)$ , and contrasted levels of environmental heterogeneity  $\sigma^2$  and  $\gamma$ . The number of infected leaves in a tree follows a Beta-Binomial distribution (Eq. (S12)) with  $\sigma^2 = 1.09$   $\sigma^2 = 1.29$ . Its density is plotted for three tree perceptions  $\gamma$ : 5.21 4.82 (estimated value on the real data set), 10 (intermediate value) and 60 for which the Beta-Binomial distribution is approaching a Binomial distribution. The number of infected leaves in a twig follows a Gamma-Binomial distribution (Eq. (S18)). Its density is plotted for three leaf suitabilities  $\sigma^2$ : 1.09 1.29 (estimated value on the real data set), 5 (a higher value) and 0.01 a value lowering variability in leaf suitability between twigs (when  $\sigma^2$  tends to 0, all twigs share the same leaf suitability).

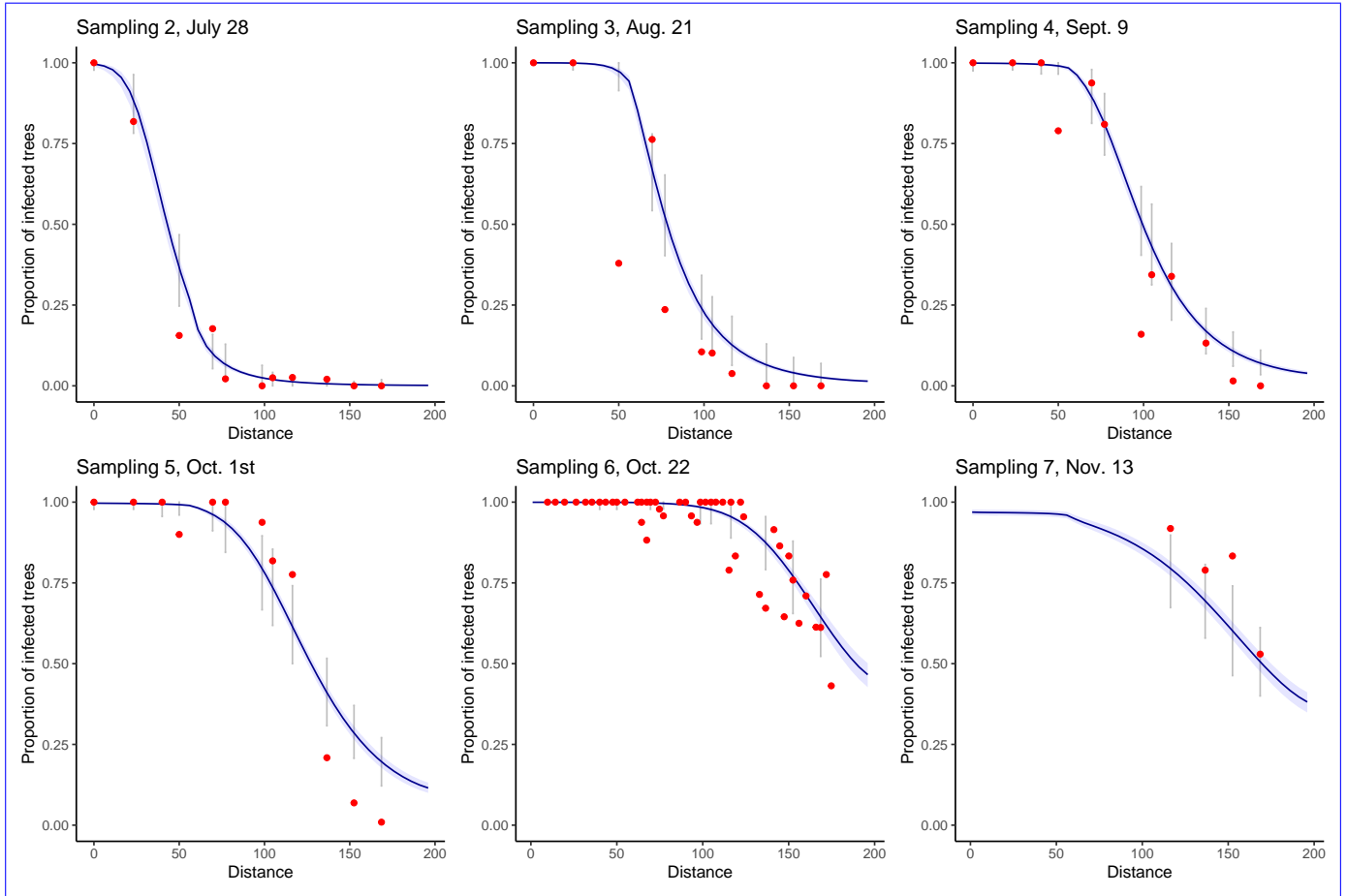


Figure 5: Model check under the selected dispersal model  $J_{\text{Exp}}$ : Coverage rates for the raw sampling. Each sampling date is represented on a separate graph. Sampling 1 is not represented because it corresponds to the initial condition of the epidemics for all simulations. Blue areas correspond to the pointwise 95% confidence envelopes for the proportion of infected trees, grey intervals correspond to the 95% prediction intervals at each site, *i.e.* taking into account the observation laws given the proportion of infected trees. Red points correspond to the observed data. Only four observations are available for sampling 7 because at this date (November 13) the leaves had already fallen from the trees located upstream the valley. The total coverage rate over all sampling dates is 0.750.71.

Appendix to: A mechanistic-statistical approach to infer dispersal  
and demography from invasion dynamics, applied to a plant  
pathogen

Méline Saubin<sup>1</sup>, Jérôme Coville<sup>2</sup>, Constance Xhaard<sup>1,2,3</sup>, Pascal Frey<sup>1</sup>, Samuel  
Soubeyrand<sup>2</sup>, Fabien Halkett<sup>1</sup> and Frédéric Fabre<sup>4</sup>

<sup>1</sup> Université de Lorraine, INRAE, IAM, F-54000 Nancy, France

<sup>2</sup> INRAE, BioSP, 84914 Avignon, France

<sup>3</sup> Université de Lorraine, INSERM CIC-P 1433, CHRU de Nancy, INSERM U1116, Nancy, France.

<sup>4</sup> INRAE, Bordeaux Sciences Agro, SAVE, F-33882 Villenave d'Ornon, France

**Corresponding author:** Meline Saubin

**Current adress:** Populationsgenetik, Technische Universität München, Liesel-Beckmann-Str. 2,  
85354 Freising, Germany

**E-mail:** meline.saubin@tum.de



## S1 Numerical scheme

We use an implicit Euler scheme combined with a finite difference scheme (see Allaire, 2005 for details) to compute the solution  $u(t, x)$  of the reaction-diffusion equation over  $[-R, R] \times [0, T]$ , with  $2 \times R$  the length of the modelled environment, and  $T$  the duration of the modelled process. For the integro-differential equation, we use an explicit Euler scheme. More precisely, we perform a standard explicit Euler time discretisation of the equation:

$$\frac{\partial u}{\partial t}(t, x) \approx \frac{u(t + \delta, x) - u(t, x)}{\delta} \quad (\text{S1})$$

that leads to:

$$\begin{aligned} u(t_{n+1}, x) = u(t_n, x) + \delta \left( \int_{-R}^R J(x-y)[u(t_n, y) - u(t_n, x)] dy \right) \\ + \delta r(x)u(t_n, x) \left( 1 - \frac{u(t_n, x)}{K} \right) \end{aligned} \quad (\text{S2})$$

where  $\{t_n = n\delta = nT/N : n = 0, \dots, N\}$  is a series of increasing times separated by  $\delta = T/N > 0$ , and  $N$  is the number of time steps in the series. For the space discretisation, we define a regular grid  $\{x_i = -R + i\varepsilon = -R + 2Ri/I : i = 0, \dots, I\}$  with  $I + 1$  points separated by  $\varepsilon = 2R/I > 0$ . We make the following approximation for all  $x$  in  $[-R, R]$ :

$$u(t_n, x) \approx \sum_{i=0}^I u(t_n, x_i) \mathbb{1}_{[x_i, x_i + \varepsilon)}(x) \quad (\text{S3})$$

where  $x \mapsto \mathbb{1}_{[x_i, x_i + \varepsilon)}(x)$  is the indicator function that gives 1 if  $x \in [x_i, x_i + \varepsilon)$ , 0 otherwise. Based on this approximation, we only need to compute  $u(t, x)$  at points  $x_i$ ,  $i = 0, \dots, I$ . Plugging Approxima-

tion (S3) in the integral of Equation (S2) computed for  $x = x_i$  yields:

$$\begin{aligned}
& \int_{-R}^R J(x_i - y)[u(t_n, y) - u(t_n, x_i)] dy \\
& \approx \int_{-R}^R J(x_i - y) \left[ \left( \sum_{j=0}^I u(t_n, x_j) \mathbb{1}_{[x_j, x_j + \varepsilon]}(y) \right) - u(t_n, x_i) \right] dy \\
& = \left( \sum_{j=0}^I u(t_n, x_j) \int_{-R}^R J(x_i - y) \mathbb{1}_{[x_j, x_j + \varepsilon]}(y) dy \right) - \left( u(t_n, x_i) \int_{-R}^R J(x_i - y) dy \right) \\
& \approx \varepsilon \left( \sum_{j=0}^I u(t_n, x_j) J(x_i - x_j) \right) - \varepsilon u(t_n, x_i) \sum_{j=0}^I J(x_i - x_j)
\end{aligned} \tag{S4}$$

Let us define the matrix  $\mathbf{J}^{in} := (J(x_i - x_j))_{0 \leq i, j \leq I}$  whose element  $(i, j)$  is  $\mathbf{J}_{ij}^{in} = J(x_i - x_j)$ . We get the following numerical scheme:

$$\begin{aligned}
u(t_{n+1}, x_i) = & u(t_n, x_i) + \delta \varepsilon \left[ \sum_{j=0}^I \mathbf{J}_{ij}^{in} u(t_n, x_j) - u(t_n, x_i) \left( \sum_{j=0}^I \mathbf{J}_{ij}^{in} \right) \right] \\
& + \delta r(x_i) u(t_n, x_i) \left[ 1 - \frac{u(t_n, x_i)}{K} \right]
\end{aligned} \tag{S5}$$

By defining the vectors  $\mathbf{U}(t_n) = (u(t_n, x_i))_{0 \leq i \leq I}$ ,  $\mathbf{R} = (r(x_i))_{0 \leq i \leq I}$  and  $\mathbf{1} = (1)_{0 \leq i \leq I}$ , we have to solve the linear system:

$$\mathbf{U}(t_{n+1}) = \mathbf{U}(t_n) + \delta \varepsilon \{ \mathbf{J}^{in} \mathbf{U}(t_n) - \mathbf{U}(t_n) \cdot (\mathbf{J}^{in} \mathbf{1}) \} + \delta \{ \mathbf{R} \cdot \mathbf{U}(t_n) \} \cdot \left\{ \left( 1 - \frac{\mathbf{U}(t_n)}{K} \right) \right\} \tag{S6}$$

where  $\cdot$  is the element-wise multiplication operator.

## S2 Distributions of the population measurements

### S2.1 Term designations for the sampling units

In our biological application, a poplar leaf represents a habitat unit, a twig represents a group of habitat units, and a tree represents a habitat bloc. For clarity, we refer to leaves, twigs and trees in the following explanations. We call a sampling site a surveyed area along the valley, containing several hundreds of trees. Further adaptations of this model to other sampling units would only require adapting this initial vocabulary (Figure 1).

### S2.2 Raw sampling

In the raw sampling, trees represent the sampling units, and  $B_{st}$  trees are observed in site  $s$  at time  $t$ . For each tree  $b \in \{1, \dots, B_{st}\}$ , we measure the presence/absence of the pathogen by monitoring an equivalent number of  $M$  leaves within  $b$  (see Appendix S3 below for the determination of  $M$ ). A tree is infected if at least one pathogen lesion has been detected, in at least one leaf of the tree. The observation in site  $s$  at time  $t$  is the number  $Y_{st}$  of infected trees.

Now, let us derive the probabilistic law of the presence/absence of the pathogen in any tree  $b$  observed in site  $s$  at time  $t$ . In this paragraph, subscripts  $s$ ,  $t$ , and  $b$  are generally omitted to avoid cumbersome notation. We first remind that the numbers of pathogen lesions  $N_i(t)$  in the leaf  $i \in \{1, \dots, M\}$  observed in tree  $b$ , given  $R_i(t)$  and  $u(t, x_s)$ , are independent and Poisson distributed (see Eq. (2) in the main text):

$$N_i(t) \mid u(t, x_s), R_i(t) \underset{\text{indep.}}{\sim} \text{Poisson}(u(t, x_s)R_i(t)) \quad (\text{S7})$$

In the raw sampling,  $M$  leaves are sampled at different locations on the tree (*i.e.* they belong to different groups, referred to as twigs), but further information about the twigs is not known. Thus, in the following, we take into account the twig structure without exploiting twig information. The leaves of a given twig  $g$  on tree  $b$  share at time  $t$  the same suitability  $\mathcal{R}_g(t)$ , which is unobserved and Gamma distributed like in Eq. (3) in the main text (for all leaves  $i$  in twig  $g$ ,  $R_i(t) = \mathcal{R}_g(t)$ ). Given the suitabilities  $\{\mathcal{R}_g(t) : g = 1, \dots, G\}$  of twigs which compose tree  $b$  and given the absence of data about the twigs,  $R_i(t)$  ( $i \in \{1, \dots, M\}$ ) are independent and identically distributed under the discrete empirical probability distribution:

$$\hat{F}_G(r) = \frac{1}{G} \sum_{g=1}^G \mathbb{1}(r \leq \mathcal{R}_g(t)) \quad (\text{S8})$$

where  $\mathbb{1}(\cdot)$  is the indicator function. Therefore,  $N_i(t)$  ( $i \in \{1, \dots, M\}$ ) given  $\{\mathcal{R}_g(t) : g = 1, \dots, G\}$  and  $u(t, x_s)$  are independent and their probability distribution is, using Eqs. (S7)–(S8):

$$P[N_i(t) = n \mid u(t, x_s), \{\mathcal{R}_g(t) : g = 1, \dots, G\}] = \frac{1}{G} \sum_{g=1}^G \exp(-u(t, x_s)\mathcal{R}_g(t)) \frac{(-u(t, x_s)\mathcal{R}_g(t))^n}{n!} \frac{(u(t, x_s)\mathcal{R}_g(t))^n}{n!} \quad (\text{S9})$$

The suitability  $\mathcal{R}_g(t)$  being Gamma distributed with shape and scale parameters  $\sigma^{-2}$  and  $\sigma^2$ , respectively, the right-hand-side of Eq. (S9) is a Monte Carlo approximation of the integral:

$$\begin{aligned} & \int_{\mathbb{R}_+} \exp(-u(t, x_s)r) \frac{(-u(t, x_s)r)^n}{n!} \frac{(u(t, x_s)r)^n}{n!} \frac{1}{(\sigma^2)^{\sigma^{-2}} \Gamma(\sigma^{-2})} r^{\sigma^{-2}-1} e^{-r/\sigma^2} dr \\ &= \frac{\Gamma(n + \sigma^{-2})}{(n!) \Gamma(\sigma^{-2})} \left( 1 - \frac{u(t, x_s)}{u(t, x_s) + \sigma^{-2}} \right)^{\sigma^{-2}} \left( \frac{u(t, x_s)}{u(t, x_s) + \sigma^{-2}} \right)^n \end{aligned} \quad (\text{S10})$$

which coincides with the probability distribution of the Negative-Binomial law (*i.e.* the Gamma-

Poisson mixture distribution) given by Eq. (4) in the main text. The larger  $G$ , the more precise the approximation. Consequently,  $N_i(t)$  ( $i \in \{1, \dots, M\}$ ) given  $u(t, x_s)$  are asymptotically independent and distributed under the Negative-Binomial distribution given by Eq. (4) in the main text. Based on this approximation, the infections of leaves from tree  $b$  in site  $s$  at time  $t$  are asymptotically independent and distributed under Bernoulli distributions with success probability:

$$\begin{aligned}
 p_{st}^{\text{leaf}} &= P(N_i(t) > 0 \mid u(t, x_s)) \\
 &= 1 - P(N_i(t) = 0 \mid u(t, x_s)) \\
 &= 1 - (1 + u(t, x_s) \sigma^2)^{-1/\sigma^2}
 \end{aligned}
 \tag{S11}$$

The people who carried out the sampling observed a number  $M$  of leaves on tree  $b$ . Due to the particular configuration of the foliage of each tree, we assumed that the number  $Y_{stb}^{\text{leaf}}$  of infected leaves among the  $M$  leaves observed in tree  $b$  is approximately distributed under a Beta-Binomial distribution with mean  $M p_{st}^{\text{leaf}}$  and tree perception parameter  $\gamma$ :

$$Y_{stb}^{\text{leaf}} \mid u(t, x_s) \sim_{\text{approx.}} \text{Beta-Binomial}(M, p_{st}^{\text{leaf}}, \gamma)
 \tag{S12}$$

Accordingly, the probability, as *perceived* by people in charge of the sampling, of leaf infection on the set of  $M$  leaves observed on a given tree, is distributed according to a Beta distribution. The Beta distribution is centred around the true probability of leaf infection  $p_{st}^{\text{leaf}}$  and allows *perceived* probability to vary from tree to tree depending on the tree perception parameter  $\gamma$ . It follows that the infection of tree  $b$  is approximately distributed under the Bernoulli distribution with success

probability:

$$\begin{aligned}
p_{st}^{\text{tree}} &= P(Y_{stb}^{\text{leaf}} > 0 \mid u(t, x_s)) \\
&= 1 - P(Y_{stb}^{\text{leaf}} = 0 \mid u(t, x_s)) \\
&= 1 - \frac{\text{Beta}[\gamma p_{st}^{\text{leaf}}, M + \gamma(1 - p_{st}^{\text{leaf}})]}{\text{Beta}[\gamma p_{st}^{\text{leaf}}, \gamma(1 - p_{st}^{\text{leaf}})]}
\end{aligned} \tag{S13}$$

where  $p_{st}^{\text{leaf}}$  is given by S11 and Beta represents the beta function. It follows that the probability distribution functions of the number  $Y_{st}^{\text{tree}}$  of infected trees among the  $B_{st}$  trees observed satisfy, for all sampling sites  $s$  and sampling times  $t$ :

$$\begin{aligned}
f_{st}^{\text{raw}}(y) &= P[Y_{st}^{\text{tree}} = y \mid u(t, x_s)] \\
&= f_{\text{Binomial}(B_{st}, p_{st}^{\text{tree}})}(y)
\end{aligned} \tag{S14}$$

where  $f_{\text{Binomial}}$  is the density of the Binomial distribution.

### S2.3 Refined sampling

In the refined sampling,  $G_{st}$  twigs (*i.e.* groups of spatially connected leaves) are sampled in site  $s$  at time  $t$ . Here, the twig information (the number of twigs and the distribution of leaves on twigs) are known but the suitability  $\mathcal{R}_g(t)$  of leaves in a twig  $g$  remains unobserved. The numbers of pathogen lesions  $N_i(t)$  in the observed leaves  $i \in \{1, \dots, M_{stg}\}$  of twig  $g$  given  $\mathcal{R}_g(t)$  and  $u(t, x_s)$  are independent and Poisson distributed:

$$N_i(t) \mid u(t, x_s), \mathcal{R}_g(t) \underset{\text{indep.}}{\sim} \text{Poisson}(u(t, x_s)\mathcal{R}_g(t)) \tag{S15}$$

Then, the numbers of infected leaves  $Y_{stg}^{\text{leaf}}$  (*i.e.* leaves with at least one pathogen lesion) given  $\mathcal{R}_g(t)$  and  $u(t, x_s)$  are independent and distributed under the following Binomial distributions:

$$Y_{stg}^{\text{leaf}} \mid u(t, x_s), \mathcal{R}_g(t) \underset{\text{indep.}}{\sim} \text{Binomial}(M_{stg}, 1 - e^{-u(t, x_s)\mathcal{R}_g(t)}) \quad (\text{S16})$$

In addition,

$$u(t, x_s)\mathcal{R}_g(t) \mid u(t, x_s) \underset{\text{indep.}}{\sim} \text{Gamma}(\sigma^{-2}, u(t, x_s)\sigma^2) \quad (\text{S17})$$

Using Eqs. (S15)–(S17),  $Y_{stg}^{\text{leaf}}$  given  $u(t, x_s)$  are independent and follow Gamma-Binomial mixture distributions:

$$\begin{aligned} f_{st}^{\text{ref}}(y) &= P[Y_{stg}^{\text{leaf}} = y \mid u(t, x_s)] \\ &= \int_0^\infty f_{\text{Binomial}(M_{stg}, 1 - e^{-z})}(y) f_{\text{Gamma}(\sigma^{-2}, u(t, x_s)\sigma^2)}(z) dz \end{aligned} \quad (\text{S18})$$

where  $f_{\text{Gamma}}$  is the density of the Gamma distribution. Note that this Gamma-Binomial mixture distribution is an over-dispersed Binomial distribution like the Beta-Binomial distribution.

### S3 Estimation of the number of leaves efficiently observed during tree scans

A problem inherent to the raw sampling design is that we do not know the number of leaves observed during the scan of the trees, contrary to the twig data for which we counted both the number of infected leaves and the total number of leaves carried by each observed twig. In other words, an inspected tree is a set of leaves of unknown size.

We assume in Eq. (S12) that the number  $Y_{stb}^{\text{leaf}}$  of infected leaves among the  $M$  leaves observed in tree  $b$  is approximately distributed under a Beta-Binomial distribution with mean  $M p_{st}^{\text{leaf}}$  and tree perception parameter  $\gamma$ . Parameter  $\gamma$  is however an unknown parameter. To overcome this parameter when calculating the average number of leaves observed per tree, we use the fact that on average the number of infected leaves is the same with a binomial distribution:

$$Y_{stb}^{\text{leaf}} \mid u(t, x_s) \sim_{\text{approx.}} \text{Binomial}(M, p_{st}^{\text{leaf}}) \quad (\text{S19})$$

From this distribution, we obtain at each site  $s$  and date  $t$  the probability  $p_{st}^{\text{tree}}$  that a tree is infected as a function of both the probability  $p_{st}^{\text{leaf}}$  that a leaf is infected and the number  $M$  of leaves



observed on a tree:

$$\begin{aligned}
p_{st}^{\text{tree}} &= P(Y_{stb}^{\text{leaf}} > 0 \mid u(t, x_s)) \\
&= 1 - P(Y_{stb}^{\text{leaf}} = 0 \mid u(t, x_s)) \\
&= 1 - (1 - p_{st}^{\text{leaf}})^M
\end{aligned} \tag{S20}$$

Thus, the number of leaves on a tree satisfies:

$$M = \frac{\log(1 - p_{st}^{\text{tree}})}{\log(1 - p_{st}^{\text{leaf}})} \tag{S21}$$

Let us use as approximations of  $p_{st}^{\text{tree}}$  the observed proportions  $q_{st}^{\text{tree}}$  of infected trees at sites  $s$  and dates  $t$ , and as approximations of  $p_{st}^{\text{leaf}}$  the observed proportions  $q_{st}^{\text{leaf}}$  of infected leaves (calculated from twig data). Then, an estimate  $\hat{\lambda}_M$  of the mean number of leaves  $\lambda_M$  by tree is given by:

$$\hat{\lambda}_M = \text{round} \left( \frac{1}{N} \sum_{i=1}^N \frac{\log(1 - q_{st}^{\text{tree}})}{\log(1 - q_{st}^{\text{leaf}})} \right) \tag{S22}$$

with  $N$  the number of pairs  $(s, t)$  (*i.e.* sampling sites and dates) displaying both tree and twig data. Proportions of infection  $q_{st}^{\text{tree}} = 1$  and  $q_{st}^{\text{leaf}} = 1$  where approximated to  $1 - 10^{-16}$  for numerical considerations. This procedure led to  $\hat{\lambda}_M = 10$ . This value may appear low. However,  $\lambda_M$  does not correspond to the actual mean number of leaves carried by an entire young tree but amounts to the mean number of leaves effectively inspected during tree scan, *i.e.* those observed as minutely as for the twig data in a limited time (see Eq. (S13)). It is important to note that for each tree the tree scan stops when an infected leaf is observed, or after 30 s of inspection. Therefore, the number of

inspected leaves per tree can be very low in highly infected sites.

For the practical identifiability studies, we set  $\lambda_M = 10$ . For parameter inference on the real data set a different value of  $(\hat{\lambda}_M)_t$  was estimated for each sampling date, from the observed proportions  $q_{st}^{\text{tree}}$  of infected trees and the observed proportions  $q_{st}^{\text{leaf}}$  of infected leaves at date  $t$  (Table S1).

Table S1: Estimated number of leaves effectively observed per tree for each sampling date  $t$ ,  $(\hat{\lambda}_M)_t$ . The values of  $(\hat{\lambda}_M)_t$  were used in the application on the real data set.

Date t	$(\hat{\lambda}_M)_t$
1	40
2	24
3	6
4	3
5	5
6	1

## S4 Simulation details

Computations were performed with the R software environment (R Core Team, 2018). The vector of initial population densities  $u(0, x)$  for  $x$  over  $[-R, R]$  was estimated from the data of the first sampling date, by fitting a general model for analysis of dose-response data (package `Drc` on R, Ritz et al., 2015). This vector of initial population densities represented the initial condition of all simulations. We modelled  $N = 1500$  time steps and  $I = 400$  points in space. Because of the numerical scheme, with these parameters the reaction-diffusion dispersal model R.D. required an upper limit for parameter  $\lambda$ : we set  $\lambda_{up} = 23$  for this model.

To fit our real case study, for all simulations we set  $R = 100$  km, for a 200 km long river valley, and the epidemic was monitored over  $T = 150$  days. We considered a shift in the environment topology at  $d = 0.31\%$  of the valley, which corresponds to the delimitation observed in the Durance River valley with the Serre-Ponçon dam at 62 km downstream of the starting point of the epidemic. Therefore, for all simulations, the two growth rates  $r_{up}$  and  $r_{dw}$  apply to continuous segments of proportions  $d$  and  $1 - d$  of the monitored space, respectively.

### S4.1 Practical parameter identifiability

Simulations were performed as follows in three steps.

**Step 1 :** Simulation of a realistic epidemic. Given a hypothetical dispersal model ( $J_{Exp}$ ,  $J_{Gauss}$ ,  $J_{ExpP}$  or R.D.), values in the parameter vector  $\theta = (\theta_r, \theta_J, \gamma, \sigma^2)$  are independently and randomly drawn from dedicated distributions encompassing a large diversity of invading scenarios and specified in Table S1. We then simulate the corresponding epidemic along the 1D spatial domain  $[-R, R]$ . This epidemic is considered ‘realistic’ if a set of requirements on the observed proportion of infected

trees  $P_{s,t}$  on the farther downstream site ( $s = R$ ) is met:

- $P_{R,30} < 0.1$  (the proportion of infected trees after one month is lower than 10%);
- $P_{R,75} < 0.5$  (the proportion of infected trees after two and a half months is lower than 50%);
- $P_{R,150} > 0.1$  (the proportion of infected trees after five months is higher than 10%);
- $P_{R,150} < 0.8$  (the proportion of infected trees after five months is lower than 80%).

Step 1 is complete once a candidate vector  $\theta$  leads to an epidemic satisfying the four conditions described above (*i.e.* the simulation of  $\theta$  and the epidemic is repeated while the four conditions are not satisfied). Thereafter, the vector finally retained in Step 1 is denoted  $\theta_{\text{true}}$ .

Table S1: Marginal distributions used to randomly sample the model parameters included in  $\theta = (\theta_r, \theta_J, \gamma, \sigma^2)$  before checking the requirements detailed in Step 1, with  $\theta_r = (r_{\text{dw}}, \omega)$  and  $\theta_J = (\lambda)$  or  $\theta_J = (\lambda, \tau)$  depending on the model.

Parameter	Distribution	Interval
$r_{\text{dw}}$	Log-Uniform	[0.01, 0.5]
$\omega$	Uniform	[-2, 34]
$\lambda$	Log-Uniform	[0.2, 5]
$\tau$	Log-Uniform	[0.2, 1]
$\gamma$	Log-Uniform	[2, 20]
$\sigma^2$	Log-Uniform	[0.01, 15]

**Step 2 :** Simulation of the sampling process. We consider a sampling design similar to our real experiment with six sampling dates and 12 sampling locations regularly spread over 150 days and 200 km, respectively ( $R = 100$  km). As for our real data, we increase the location density for the fifth date, with 45 locations instead of 12. For each date and location, the raw sampling consists in simulating the observed sanitary status of 10 leaves per tree from 100 trees, and the refined sampling consists in simulating the observed sanitary status of 25 spatially connected leaves from 20 twigs,

the simulations being performed given  $\theta_{\text{true}}$ . The resulting data set is denoted  $\mathcal{D}_{\text{true}}$ .

**Step 3 :** Parameter estimation. We use the data  $\mathcal{D}_{\text{true}}$  to estimate the model parameters by minimizing the logarithm of the likelihood function  $L(\theta)$ . In our case, preliminary tests revealed that classical optimisation algorithms were not accurate enough to provide satisfactory rates of convergence due to local optimum problems. Thus, we adopt a hybrid strategy combining first a Nelder-Mead algorithm (improving global search ability) and then a Nlminb algorithm (for its high computational efficiency). Specifically, we proceed in three substeps described below, the crucial stage consisting in finding initial values that give a satisfactory rate of convergence.

**Step 3.1 :** Using Step 1, we generate 500 vectors  $\theta_{\text{init}}$ . Note that this step was only performed once for all the estimations performed in this article. We provide in Figure S1 a comparison of the initial distribution of parameters as stated in Table S1, and of the distribution of parameters in the vector  $\theta_{\text{init}}$ , *i.e.* leading to “realistic” epidemics.

**Step 3.2 :** The corresponding 500 likelihood values  $L(\theta_{\text{init}})$  are calculated given  $\mathcal{D}_{\text{true}}$ . Then, the 20 vectors  $\theta_{\text{init}}$  corresponding to the 20 largest likelihood values are used as initial values for 50 steps of a NELDER-MEAD optimisation routine (R function `optim`), resulting in 20 updated initial parameter vectors  $\theta_{\text{init}2}$  depending on  $\mathcal{D}_{\text{true}}$ . The new initial vectors  $\theta_{\text{init}2}$  that do not satisfy lower bounds  $\theta_{\text{low}}$  and upper bounds  $\theta_{\text{up}}$  are excluded. We used  $\theta_{\text{low}} = (r_{\text{dw}} = 0.001, \omega = -7, \lambda = 0.02, \tau = 0.02, \gamma = 1.05, \sigma^2 = 10^{-7})$  and  $\theta_{\text{up}} = (r_{\text{dw}} = 0.5, \omega = 3, \lambda = 10, \tau = 1, \gamma = 30, \sigma^2 = 20)$   $\theta_{\text{up}} = (r_{\text{dw}} = 0.5, \omega = 4, \lambda = 10, \tau = 1, \gamma = 30, \sigma^2 = 20)$  with  $\lambda = 23$  in  $\theta_{\text{up}}$  instead of 10 for the R.D. model. The validity intervals defined by  $\theta_{\text{low}}$  and  $\theta_{\text{up}}$  encompass the intervals used to simulate  $\theta$  (see Table S1). The likelihood values of the  $n_{\text{init}}$  remain-

ing vectors  $L(\theta_{\text{init}2})$  are calculated (given  $\mathcal{D}_{\text{true}}$ ) and ranked in descending order.

**Step 3.3 :**  $\theta$  is then estimated using the NLMINB optimisation routine with lower and upper bounds  $\theta_{\text{low}}$  and  $\theta_{\text{up}}$ , respectively. The initial parameter values are set to the first vector  $\theta_{\text{init}2}$  as ordered in the previous step. The estimated parameter values, say  $\theta_{\text{estim}}$ , are accepted if the `nlmminb` function in R delivered a successful convergence diagnostic (with tuning parameters `rel.tol`= $5 \cdot 10^{-5}$  and `iter.max`=3000). If not, the second vector  $\theta_{\text{init}2}$  is used, and so on until reaching convergence or testing the  $n_{\text{init}}$  initial vector's values selected at step 3.2. In the latter case, a convergence failure is obtained. Overall, this algorithm allows to obtain high rates of convergence.

These three steps were reiterated until deriving the estimation of  ~~$n = 100$~~   $n = 160$  realistic epidemics for each dispersal model. Checking for practical identifiability of parameters basically relies on plotting for each dispersal model the cloud of points between  $\theta_{\text{true}}$  and  $\theta_{\text{estim}}$  (Figures S2, S3, S4, S5) and computing the corresponding correlations. Among all simulations performed, the proportions of convergence were ~~0.91, 0.95, 0.93, and 0.90~~ 0.98 for dispersal  $J_{\text{Exp}}$ ,  $J_{\text{Gauss}}$ ,  ~~$J_{\text{ExpP}}$~~ , and R.D. ~~, respectively~~ and up to 0.99 for  $J_{\text{ExpP}}$ . A simulation converged when the convergence diagnostic of the algorithm indicated a convergence, and when all parameters were estimated inside intervals defined by  $\theta_{\text{low}}$  and  $\theta_{\text{up}}$ . In the small number of simulations where the value of  $\lambda_{\text{estim}}$  proposed by the optimisation algorithm was higher than 23 (which is the upper limit of our numerical scheme, Appendix S1), the simulation was still considered convergent with  $\lambda_{\text{estim}} = 23$ . This configuration can occur in particular when trying to fit dispersal R.D. on datasets simulated according to  $J_{\text{ExpP}}$ .

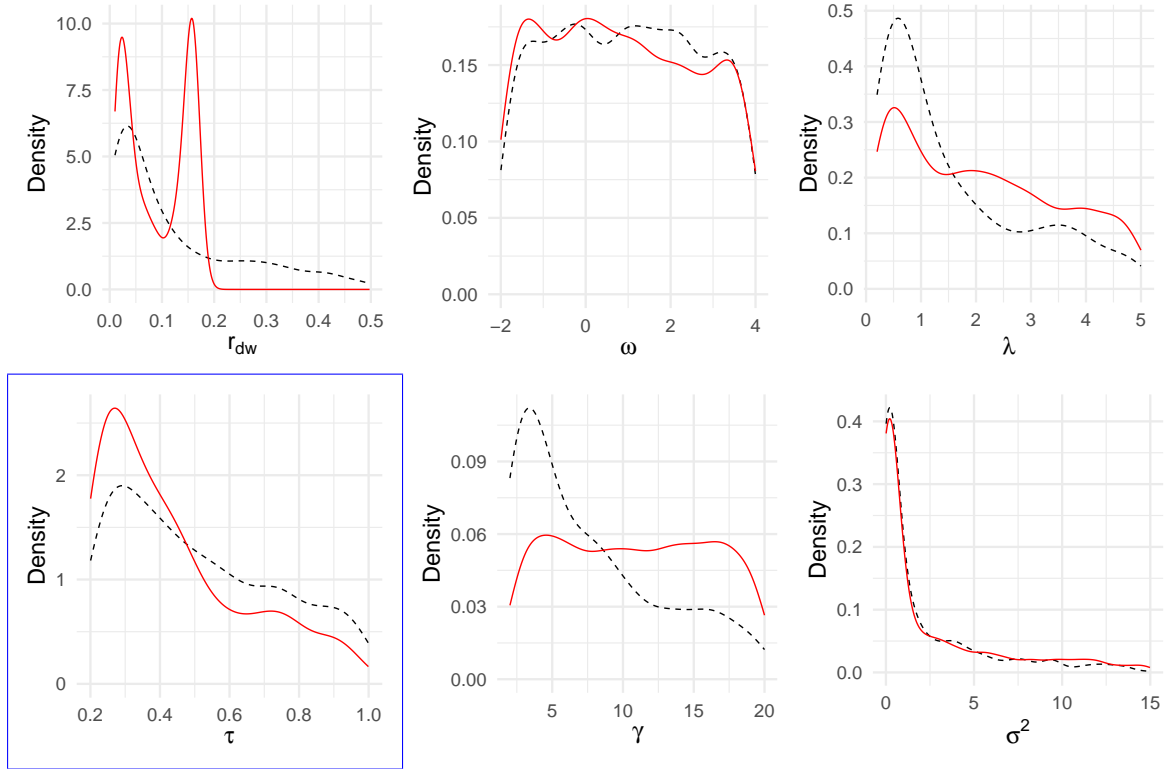


Figure S1: Distributions of parameters, before (in dotted black) and after (in red) retaining only parameters values leading to “realistic” epidemics. Dotted black distributions correspond to distributions given by Table S1. Red line distributions correspond to the distribution of parameters in  $\theta_{\text{init}}$ . We represent here the distribution of “realistic” epidemics from the four hypothetical dispersal models ( $J_{\text{Exp}}$ ,  $J_{\text{Gauss}}$ ,  $J_{\text{ExpP}}$  and R.D.) for parameters  $r_{\text{dw}}$ ,  $\omega$ ,  $\gamma$  and  $\sigma^2$ , for  $J_{\text{ExpP}}$  for parameter  $\tau$ , and for  $J_{\text{Exp}}$ ,  $J_{\text{Gauss}}$  and  $J_{\text{ExpP}}$  for parameter  $\lambda$ .

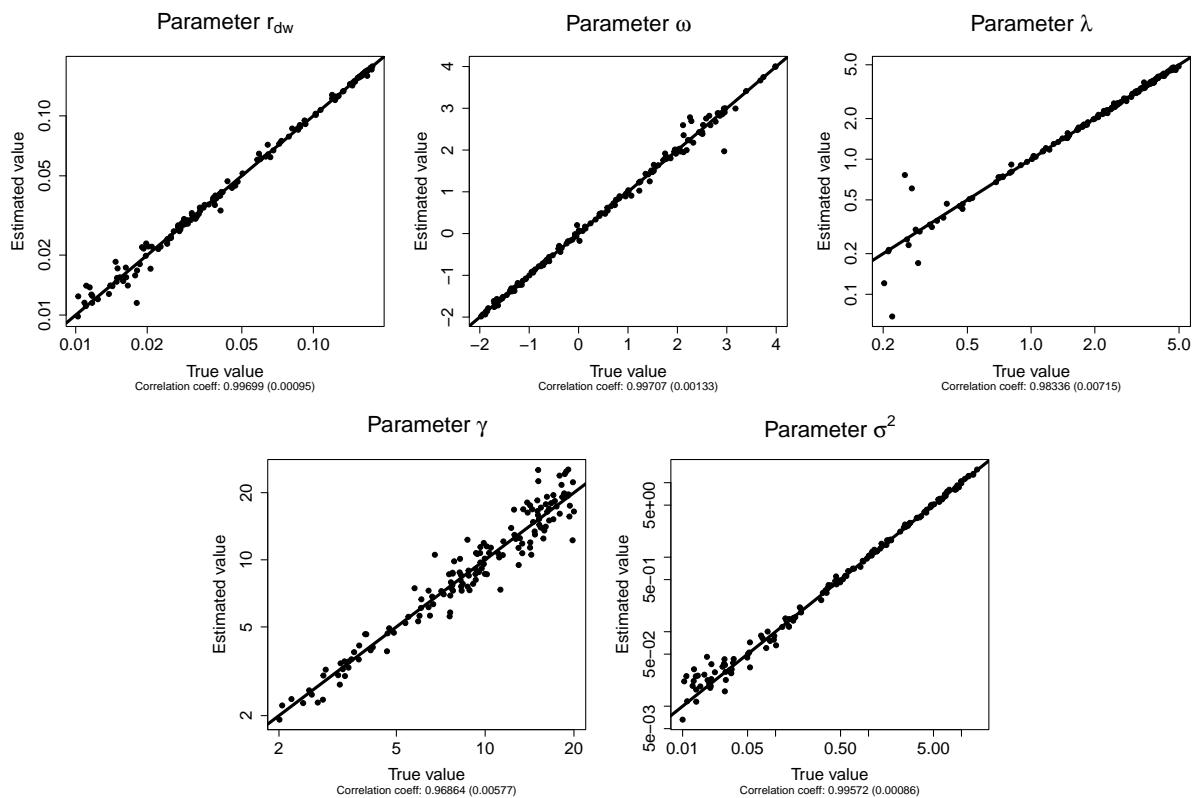


Figure S2: Practical parameter identifiability for the dispersal model  $J_{Exp}$ . Each point represents the parameter estimation ('Estimated' value) depending on the real parameter ('True' value). Each graph regroups the results of ~~100~~ 160 replicates. Straight lines correspond to the first bisector.



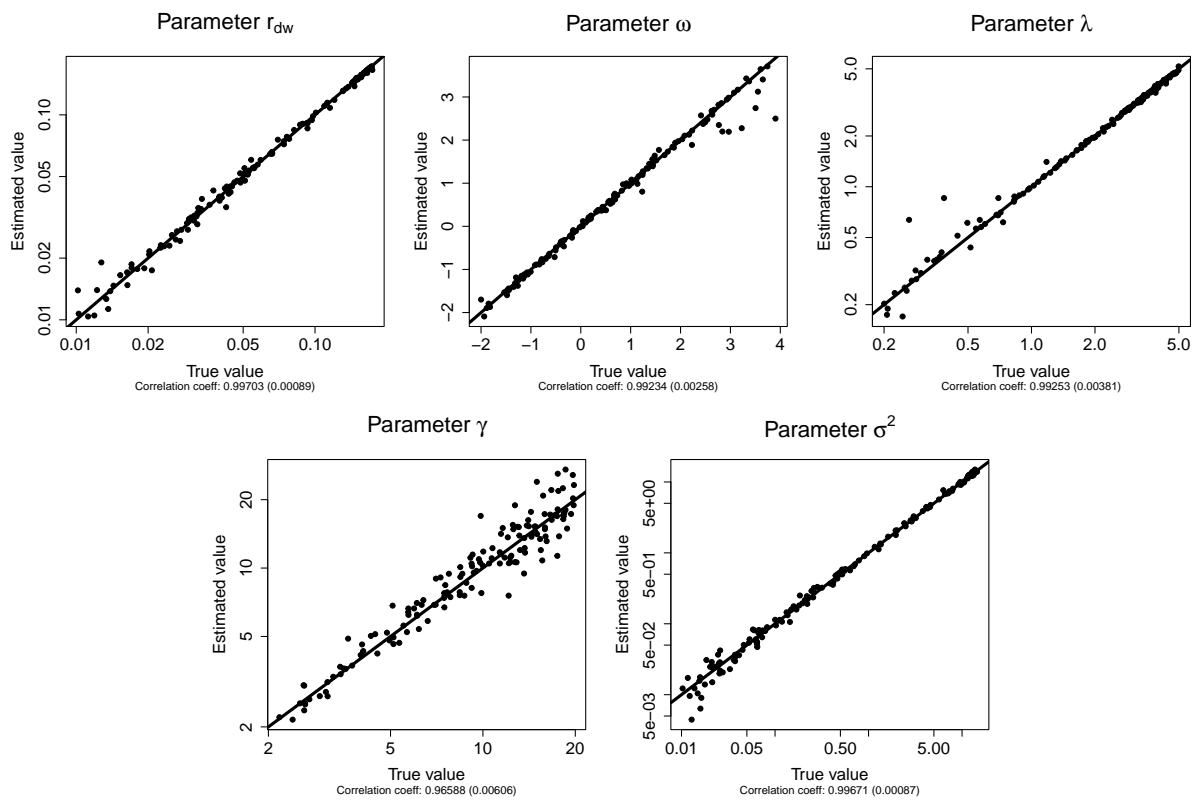


Figure S3: Practical parameter identifiability for the dispersal model  $J_{\text{Gauss}}$ . Each point represents the parameter estimation ('Estimated' value) depending on the real parameter ('True' value). Each graph regroups the results of ~~100~~ 160 replicates. Straight lines correspond to the first bisector.

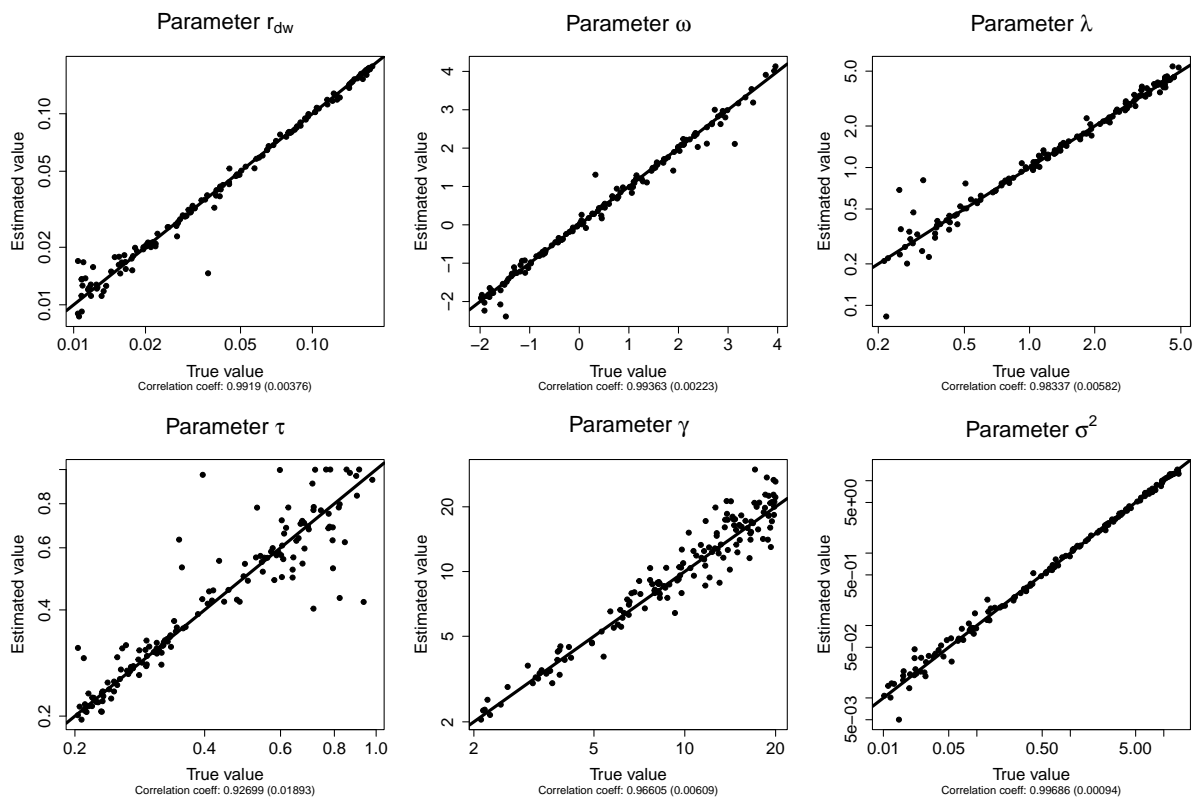


Figure S4: Practical parameter identifiability for the dispersal model  $J_{\text{ExpP}}$ . Each point represents the parameter estimation ('Estimated' value) depending on the real parameter ('True' value). Each graph regroups the results of ~~100~~ 160 replicates. Straight lines correspond to the first bisector.

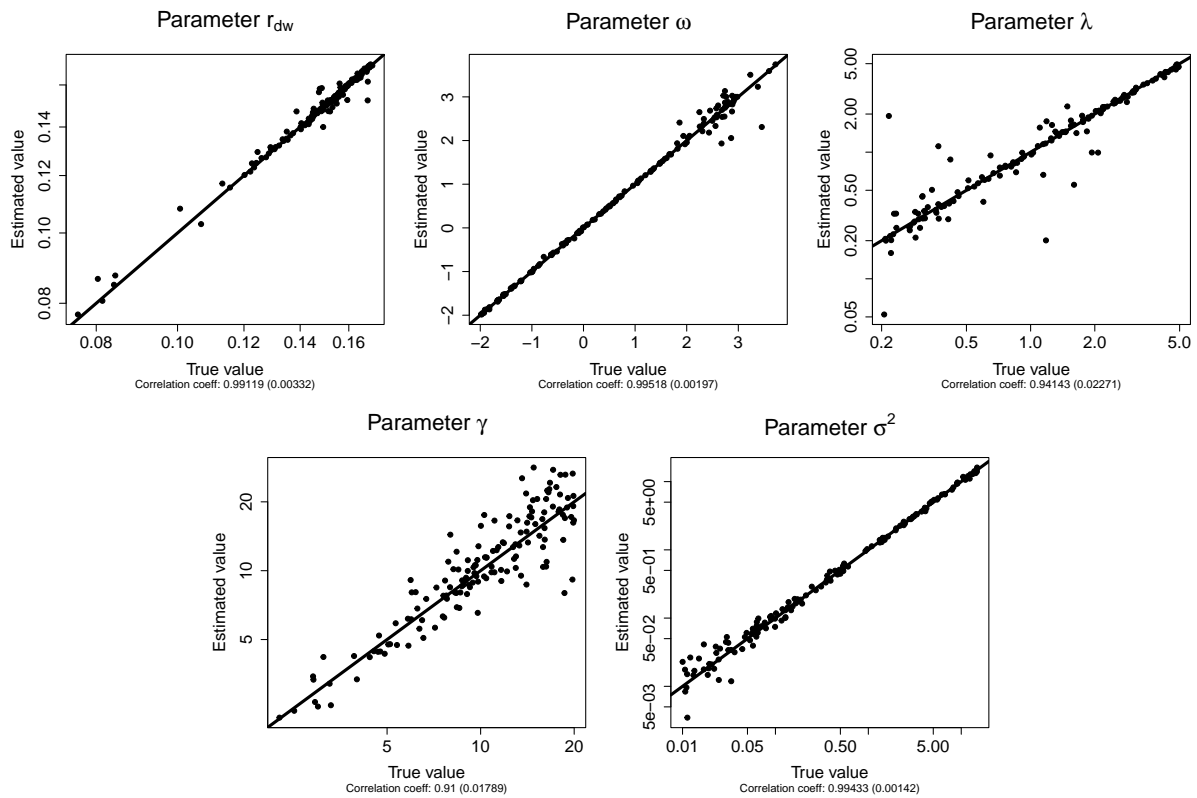


Figure S5: Practical parameter identifiability for the dispersal model R.D. Each point represents the parameter estimation ('Estimated' value) depending on the real parameter ('True' value). Each graph regroups the results of ~~100~~ 160 replicates. Straight lines correspond to the first bisector.

## S4.2 Model selection

Model practical identifiability was carried out in a similar way than parameter practical identifiability (Appendix S4.1), except that we fitted to each data set the true model (as previously) but also the three other models corresponding to the alternative hypotheses on the dispersal process. Models were compared using AIC (Akaike Information Criteria) to select the best data-supported model. AIC were assessed as  $2k - 2\ln(L)$  where  $k$  is the number of parameters of the model considered and  $L$  is the maximized value of the likelihood function. To gain more insights into the confidence level in model selection, we also calculated for each data set the difference between the AIC of the model selected and the AIC of the second-best model according to the two possible issues of the selection procedure: (i) when the model selection procedure was successful (*i.e.* the selected model was the true model) and (ii) when the model selection procedure was incorrect (*i.e.* the true model was not selected). The mean of these values were reported as  $dAIC_{\text{true}}$  and  $dAIC_{\text{wrong}}$  in Table 2. The steps were reiterated until the estimation of  $n = 50$  realistic epidemics for each dispersal model.

## S4.3 Parameter inference on the real data set

The model selection procedure was applied to the real data set by fitting four dispersal process hypotheses ( $J_{\text{Exp}}$ ,  $J_{\text{Gauss}}$ ,  $J_{\text{ExpP}}$  and R.D.). The same optimisation routines described in Appendix S4.1 were performed from five initial parameter values selected as in Step 3.2 (Appendix S4.1). The selected model corresponds to hypothesis  $J_{\text{ExpP}}$ . For parameter estimations, we used the `mle2` function from the R package `bbmle`, with method Nelder-Mead and optimizer NLMINB, to obtain maximum likelihood estimates of the vector of parameters  $\hat{\theta}$  and of its matrix of variance-covariance  $\hat{\Sigma}$ . We used as initial parameter values the vector of parameters  $\theta$  giving the lowest AIC value in the

previous model selection procedure. Confidence intervals were derived from 1,000 random draws from the multivariate normal distribution with parameters  $\hat{\theta}$  and  $\hat{\Sigma}$ . The 95% confidence intervals of each parameter is obtained using the quantiles 2.5% and 97.5% (Table 4).

#### S4.4 Model check

The model was checked by assessing the coverage rate of the data from the 95%-prediction intervals. The coverage rate was estimated as the proportion of observed data from the raw sampling within the prediction intervals (Figure 5).

Data from the raw sampling represent 97 counts  $Y_{st}$  of infected trees at sites  $s \in \{1, \dots, S\}$  (with  $S = 12$  or  $S = 45$  depending on the sampling date) and times  $t \in \{1, \dots, 6\}$ . Let us recall that, as stated in Appendix S2,  $Y_{st}$  follows a combination of Poisson and Beta-Binomial distributions whose parameters depend on the known mean value  $(\lambda_m)_t$  and the unknown  $u(t, x_s)$ ,  $\gamma$  and  $\sigma^2$ , and that  $u(t, x_s)$  is a deterministic function of dynamical parameters  $r$ ,  $\lambda$  and  $\tau$ .

Prediction intervals were calculated at each date and each site with a two-step procedure:

**Step 1** A confidence interval was obtained from 1000 random draws from the multivariate normal distribution with  $\hat{\theta}$  and  $\hat{\Sigma}$ .

**Step 2** The mean proportions of infected trees were calculated at each date and site date from each random draw of parameters obtained from Step 1. A prediction interval was obtained from these parameters given the probabilities of infection, with 1,000 random draws in the observation laws.

Model checks were performed for each dispersal kernel model, and not only the selected model  $J_{\text{ExpP}}$ , to ensure that the coverage rates were higher with the selected model (Figure 5 for the selected dispersal model  $J_{\text{ExpP}}$ , and Figures S6 and S7 for dispersal models  $J_{\text{Exp}}$  and  $J_{\text{Gauss}}$ , respectively). The

model check was not performed for dispersal model R.D. because the estimated dispersal distance  $\lambda_{\text{estim}}$  reached the upper limit of our numerical scheme  $\lambda_{\text{up}} = 23$  and did not allow to calculate the confidence intervals.

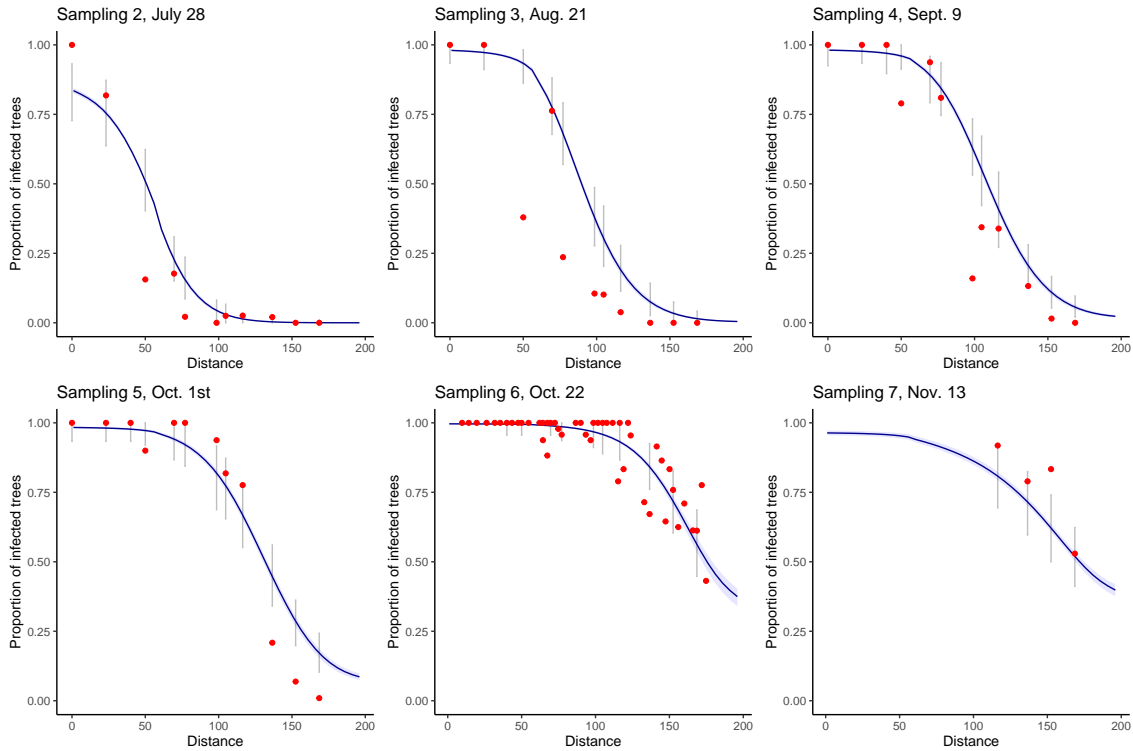


Figure S6: Model check under the dispersal model  $J_{\text{Exp}}$ : Coverage rates for the raw sampling. Each sampling date is represented on a separate graph. Sampling 1 is not represented because it corresponds to the initial condition of the epidemics for all simulations. Blue areas correspond to the pointwise 95% confidence envelopes for the proportion of infected trees, grey intervals correspond to the 95% prediction intervals at each site, *i.e.* taking into account the observation laws given the proportion of infected trees. Red points correspond to the observed data. Only four observations are available for sampling 7 because at this date (November 13) the leaves had already fallen from the trees located upstream the valley. The total coverage rate over all sampling dates is  $0.690.68$ .

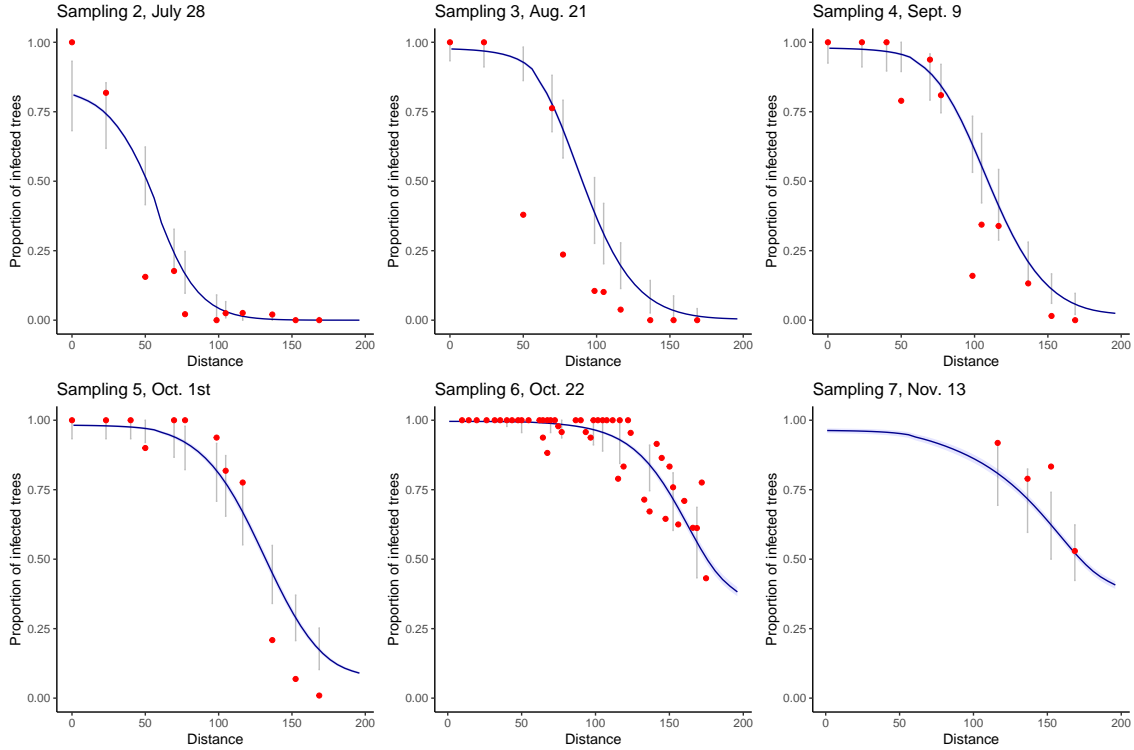


Figure S7: Model check under the dispersal model  $J_{\text{Gauss}}$ : Coverage rates for the raw sampling. Each sampling date is represented on a separate graph. Sampling 1 is not represented because it corresponds to the initial condition of the epidemics for all simulations. Blue areas correspond to the pointwise 95% confidence envelopes for the proportion of infected trees, grey intervals correspond to the 95% prediction intervals at each site, *i.e.* taking into account the observation laws given the proportion of infected trees. Red points correspond to the observed data. Only four observations are available for sampling 7 because at this date (November 13) the leaves had already fallen from the trees located upstream the valley. The total coverage rate over all sampling dates is 0.67.

## S4.5 Sampling densification

As in Appendix S4.2, numerical simulations were run to disentangle the true dispersal process from alternative dispersal processes, with densification of time and site for the raw and the refined sampling. Simulations were run with 21 sampling dates instead of 6, which amounts to one sampling every week. The number of sampling sites was set to 45 for all sampling dates. The steps described in Appendix S4.1 and S4.2 were reiterated until the estimation of  $n = 50$  realistic epidemics for each dispersal model.

Table S2: Efficiency of model selection for the densification of time samples (21 instead of 6) and the site sampled (45 instead of 12). The four first columns indicate the proportion of cases, among 50 replicates, where each tested model was selected using AIC, given that data sets were generated under a particular model (*i.e.* true model). Column  $dAIC_{\text{true}}$  (*resp.*  $dAIC_{\text{wrong}}$ ) indicates the mean difference between the AIC of the model selected when the model selected is the true one (*resp.* when the model selected is not the true model) and the second best model (*resp.* being the true model or not).

True Model	Selected Model				$dAIC_{\text{true}}$	$dAIC_{\text{wrong}}$
	$J_{\text{Exp}}$	$J_{\text{Gauss}}$	$J_{\text{ExpP}}$	R.D.		
$J_{\text{Exp}}$	<b>0.72</b> 0.64	0.060.18	0.160.12	0.06	3.235.60	1.052.02
$J_{\text{Gauss}}$	0.220.14	<b>0.60</b> 0.8	0.040	0.140.06	7.339.93	1.671.51
$J_{\text{ExpP}}$	0.120.1	0.060.02	<b>0.82</b> 0.86	00.02	<b>1788.56</b> 2228.45	2.721.81
R.D.	0.10.12	0.280.16	0.020	<b>0.60</b> 0.72	27.0132.97	0.941.04

## S5 Carrying capacity of poplar leaves

We measured the area of 10 wild poplar leaves (*Populus nigra*) and obtained a mean leaf area of  $870 \text{ mm}^2$ . We consider that poplar rust can not infect the leaf veins and edges, which represent approximately 15% of the leaf area. This leads to a net leaf area accessible to the pathogen of  $740 \text{ mm}^2$ . The size of a poplar rust lesion ranges from  $0.2 \text{ mm}^2$  to  $0.8 \text{ mm}^2$  (Maupetit et al., 2018). The lesions cannot fuse and are surrounded by living host tissue. We thus consider a lesion occupies a total area of  $1 \text{ mm}^2$ . This leads to a maximum of 740 lesions per leaf on average. To respect this order of magnitude, we consider in this analysis that the carrying capacity of a poplar leaf is 750 poplar rust lesions.



## References

- Allaire, G. (2005). *Analyse numérique et optimisation : une introduction à la modélisation mathématique et à la simulation numérique*. Editions Ecole Polytechnique.
- Maupetit, A., Larbat, R., Pernaci, M., Andrieux, A., Guinet, C., Boutigny, A. L., Fabre, B., Frey, P., and Halkett, F. (2018). Defense compounds rather than nutrient availability shape aggressiveness trait variation along a leaf maturity gradient in a biotrophic plant pathogen. *Frontiers in Plant Science*, 9.
- R Core Team (2018). R: A language and environment for statistical computing.
- Ritz, C., Baty, F., Streibig, J. C., and Gerhard, D. (2015). Dose-Response analysis using R. *PLoS One*, 10(12).